Institut National de Recherche et de Sécurité

Operation and performances of the CAIMAN facility for nanoparticle aerosol generation

NS 292 NOTE SCIENTIFIQUE ET TECHNIQUE

Table of contents

Table of illustrations

Notations

The units shown in brackets are those used in this document, and not necessarily those adopted by International System.

C_M	mass concentration (mg/m^3)
C_N	number concentration (#/cm^3)
CMMD	count median mobility diameter (nm)
e	elementary charge (e=1.602·10^{-19} C)
f	spark-discharge frequency (Hz)
I	current (fA)
P	pressure (bar)
$\overline{p}$	mean charge per particle (-)
Q	volumetric flow rate (L/min)
T	temperature (°C)
ω	spark-discharge frequency indication (arbitrary units, a.u.)
σ_g	geometric standard deviation, GSD (-)

Acknowledgements

Authors would like to thank S. Veissiere from Laboratory of Inorganic Analysis and Aerosol Characterization (INRS) for imaging support. Jonathan Jacoby contributed actively to the technical work and data analysis during his work experience as a master 2 student “Physique et Matériaux - Physique de la matière condensée”, University of Metz (57).

1. Introduction

Rationally designed, manufactured nano-objects (nanoparticles and nanostructured particles – NP) attract a great deal of interest, due to their many technologically interesting properties. The properties of NP and their applications have given birth to technological and economic expectations for industries using NP or materials/end products containing NP (nanomaterials). However, some of these properties have given rise to concern that they may be harmful to humans.

In the workplaces where NP are manufactured or used, exposure to airborne NP is plausible at all phases of the nanomaterial life cycle, although the nature, level of exposure and the number of person involved could differ greatly. One major uncertainty in the health risk assessment of NP arises from the lack of knowledge of their physicochemical properties and behavior in the airborne state (aerosol phase). Among the technical challenges ahead for assessing workers exposures to NP are to:

(a) redesign and evaluate "NP-capable" instruments already in laboratory use into portable and affordable devices, and

(b) expand the sensing technology available for NP detection by adopting new options with realistic potential for real-time measurement and compact design.

The present report describes the nanoparticle generation facility in aerosol phase called "**CAIMAN**" (acronym for **C**haracterization of **A**erosol **I**nstrumentation devoted for **M**easuring **A**erosols of **N**anoparticles) and its performances that has been developed to produce well-defined nanoaerosols.

2. Description of the experimental setup (CAIMAN)

CAIMAN (for '**C**haracterization of **A**erosol **I**nstrumentation devoted for **M**easuring **A**erosols of **N**anoparticles') is a versatile experimental facility that was designed and built to generate stable and reproducible aerosols of nanoparticles (nanoaerosols) with controlled properties (concentration, size, shape, mean charge level). It was initially developed in a collaborative research work within the Aerosol Physics and Metrology Laboratory from the Institut de Radioprotection et de Sûreté Nucléaire (IRSN) and the Aerosol Metrology Laboratory from INRS, which holds the non-transportable facility in its research centre near Nancy, France.

Within CAIMAN, the particle-free air introduced into different points of the set-up comes from a purification unit (TSI model 3074B), and the excess aerosol is filtered by means of HEPA filters (CAMFIL, model 'filtre BAG').

Figure 1 shows a schematic of the CAIMAN experimental facility in its standard configuration. A different arrangement has been used for producing mixture of NP and particles representing background aerosols (see paragraph 3.7 page 50).

Table 1 gathers the range of each of the mass flow meters disposed within CAIMAN.

Table 1 : Characteristics of the mass flow meters within CAIMAN

Flow meter	Regulation ?	Range (L/min)
❶	No	0 – 50
❷	No	0 – 20
❸	No	0 - 100
❹	Yes	0 – 100
❺	Yes	0 - 50

Following sections briefly describe each of the elements constituting the CAIMAN facility, i.e. an airborne NP generator, a bipolar ion generator, a high-temperature furnace and a home-made ageing volume.

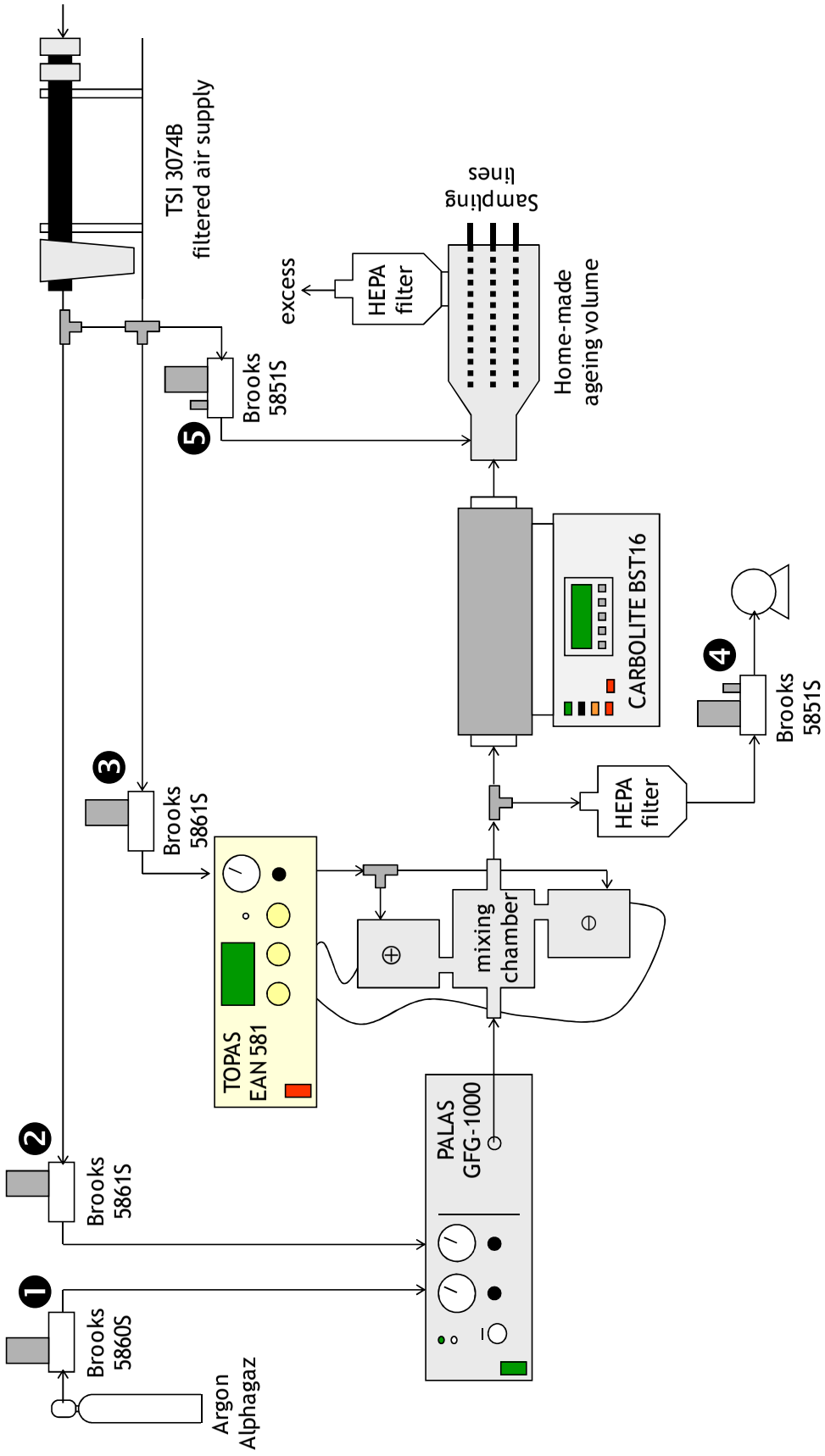

Figure 1: Schematic of the CAIMAN facility in its standard configuration

2.1. Airborne NP generation

Within CAIMAN, airborne NP are produced by means of a spark-discharge generator (GFG-1000, PALAS). The production of airborne NP by spark discharge has been studied extensively by several authors in different situations [1-15].

In the PALAS GFG-1000 generator, electrode material is evaporated in the vicinity of the spark. Material vapor nucleates/condenses to the solid phase, forming very small primary particles which then coagulate according to particle number concentration and operating conditions. These mechanisms can be to some extent controlled by varying the flow rates of argon shielding and primary dilution by air. Aerosol production rate varies by adjusting the spark-discharge frequency ω[1] which is directly controlled by the potentiometer setting of the GFG-1000 PALAS. Consequently, this NP generation system allows a variation of both the **particle concentration** (via the argon and air flow rates, spark-discharge frequency) and their **chemical nature** by changing the material of the electrodes. Presently, seven different electrode materials have been studied, which chemical composition was determined by ICP-MS and gathered in Table 2.

Table 2 : Characteristics of the electrodes used within the NP generator

Electrode	Composition
Carbon[2]	Graphite (pure)
Aluminum (type 2071A)	Al(93.1%) – Cu(4.8%) – Fe(0.7%) – Mn(0.6%) – Si(0.5%) – Mg(0.3%)
Copper	Cu(99.45%) - Al(0.5%) – Si(0.04%)
Silver[3]	Ag > 99.99%
Constantane[3]	Cu(55%) – Ni(45%)
Cu/Be[3]	Cu(98%) – Be(1.9%) – Co(0.2%) – Pb(0.3%)
Cu/Co/Be[3]	Cu(95.6%) – Be(0.5%) – Co(2.4%)

[1] The spark-discharge frequency indication, notated ω, corresponds to the parameter set on the potentiometer. The real sparking frequency f is then given by $f = 0.3\ \omega$ (PALAS documentation).

[2] Delivered by PALAS.

[3] Delivered by Goodfellow.

2.2. Airborne NP state-of-charge

To cover a wide range of **electrical mean charge level**, a bipolar ion generator (EAN 581, TOPAS) is included in CAIMAN at the outlet of the NP generator. Its principle is based on air ionisation by corona charging in two independent chambers. Positive and negative ions can be produced separately in each chamber, and then mixed consecutively with the particles within a mixing chamber which geometry was optimised to increase particle charging efficiency. Both the air flow rate and the corona charger parameters (voltage and current) can be adjusted, allowing a wide range of NP electrical state-of-charge. Further elements can be found in the work of Marquard *et al.* [16, 17] in unipolar mode.

2.3. Airborne NP morphology

Morphology being another key-parameter of the NP produced within CAIMAN, a high-temperature furnace (CARBOLITE BST16 – maximum operating temperature 1500°C) was inserted in the facility. Indeed, several studies [18-28] have shown particle restructuration by sintering under high temperatures. The high-temperature furnace can be operated at different temperatures to provide either partial sintering of agglomerates or coalescence, allowing some degree of control over particle morphology of particles with constant chemistry.

2.4. Airborne NP sampling and measurement

The aerosol leaving the furnace is allowed to age in a 2-liter volume located at the end of the facility (see Figure 1) from which airborne NP can be **sampled and diluted** by means of an additional air flow injected at the outlet of the device. It should be noted that this ageing volume is equipped with **four sampling lines in parallel**, which allows simultaneous measurements. Obviously, more instruments can be connected if flow splitters are put into line. For testing with monodisperse particles, a DMA can be connected at one of the four outputs. Connections are in metric but any other connections can easily be used.

It should be noted that CAIMAN can only be used with **aspirating aerosol instruments**.

2.5. Safety issues

Due to strong nuclear safety regulation in France, no radioactive source can be brought to the Institute. The only radioactive source hold by the Aerosol Metrology Laboratory is an Am^{241} sealed source devoted to the Grimm DMA.

The entire CAIMAN facility is confined as shown in Figure 2.

The first part of the facility is contained within a box containment system (4m x 0.8m x 0.8m) that limits any worker exposure from accidental release from the generator to the entrance of the ageing chamber. The second part of the facility is located within a constant velocity 2-m large fume hood.

Figure 2: Picture of the CAIMAN facility

3. Features of CAIMAN

In this section, key properties of the aerosols of NP produced within CAIMAN are exposed.

Two operating configurations were tested for each electrode material, as stated in Table 3 (subscripts 1, 2 and 5 refer to the mass flow meters indexes attributed in Figure 1).

Table 3: Configurations tested for characterizing CAIMAN

Configuration	P_{Ar}[4] (bar)	Q_1 (L/min)	P_{air}[4] (bar)	Q_2 (L/min)	Q_5 (L/min)
1	1	2.5	0	0	10
2	1	2.5	1	20	10

Electronic diffraction and EDS have been used to provide the oxidation state of the aerosol produced. When using aluminum and copper as material electrode, the aerosol produced is composed respectively of Al_2O_3 and Cu_2O particles. When using silver as material electrode, the aerosol produced is composed of Ag particles.

For constantane and both electrodes containing Beryllium, chemical analysis was not performed. Furthermore, concerning Be wires, only configuration 1 was investigated.

3.1. Generation stability

Before comprehensive characterization of the airborne NP produced within CAIMAN, the generation stability was tested over 170 minutes for carbon electrodes in configuration 2 and ω = 1000 a.u. The 46 scans measured by the SMPS showed a variation of ± 12 % in terms of count median mobility diameter (CMMD) relative to its mean value over all scans ($\overline{CMMD}$) as calculated by:

$$ratio = \frac{CMMD(scan\ i)}{\overline{CMMD}(all\ scans)}$$

The Figure 3 shows the results obtained.

[4] The pressures of Argon and dilution air are the parameters set on the generator, and correspond to the flow rates indicated in Table 3, they were measured and controlled during the experiments.

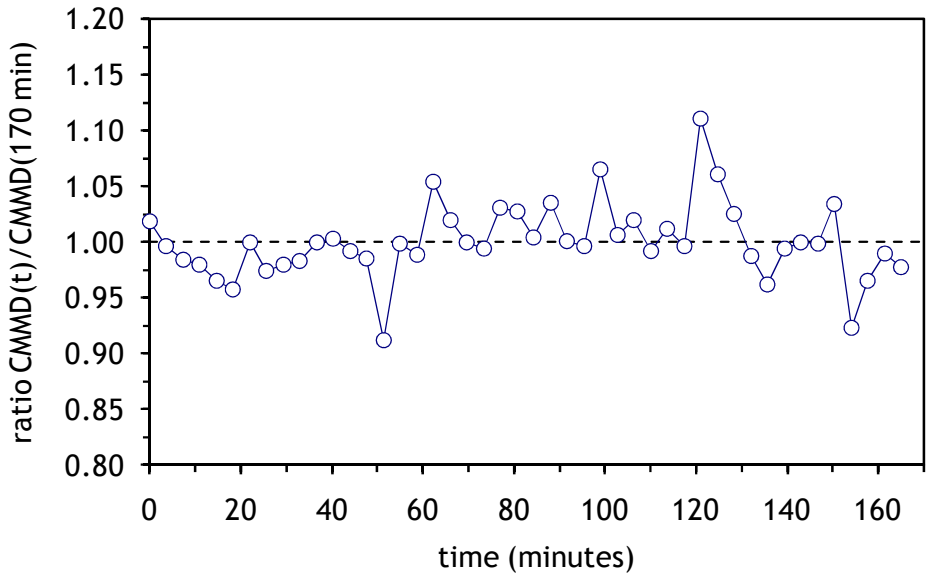

Figure 3: Evolution of CMMD for Carbon electrodes in configuration 2 and ω = 300 over 170 minutes

The mass concentration of the aerosol produced was also monitored by means of a TEOM microbalance, leading to a variability of ± 15 % during a measurement period of 1 hour, as shown in Figure 4.

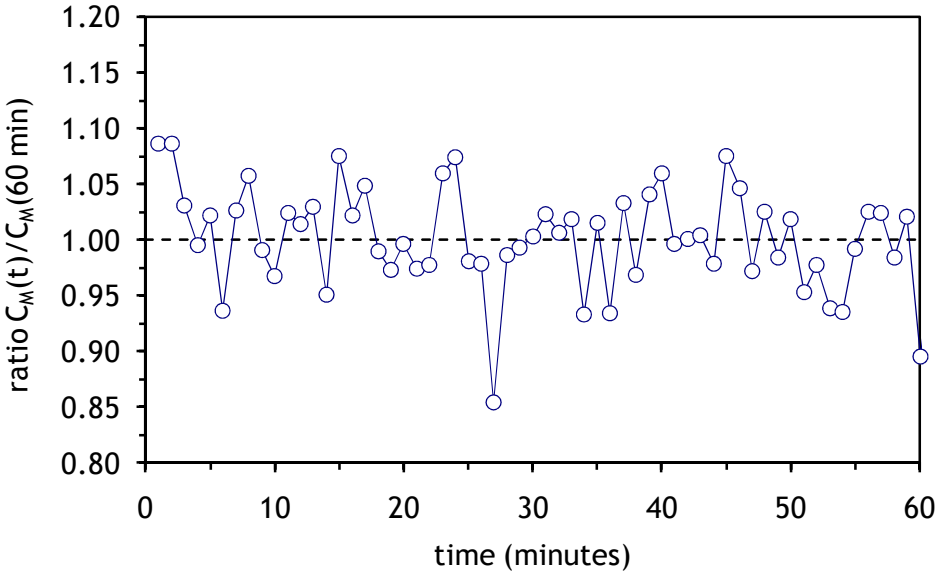

Figure 4: Evolution of mass concentration for Carbon electrodes in configuration 2 and ω = 300 over 60 minutes

In terms of total number concentration of airborne NP, variations below 4 % were observed over 4 hours of generation.

Furthermore, reproducibility of the generation was tested (same operating parameters set with one week delay) and showed a close agreement between NP size distributions (less than 10 % variation in terms of total concentration and CMMD).

3.2. Number size distributions

The size distribution of the generated airborne NP was measured by a SMPS system (GRIMM SMPS+C, composed of a DMA 'Vienna Type' and a CNC model 5.403) operating at a flow rate of 0.3 L/min. This system allows the measurement of the number of particles according to their electrical mobility diameter (from 5.5 to 350 nm with the middle size DMA, and from 11 to 1080 nm with the long DMA). The choice of the DMA was adapted depending on the median size of the aerosols measured to provide most of the distribution.

Figure 5 shows a schematic of the set-up adopted for the measurement of the size distributions of the aerosols produced within CAIMAN.

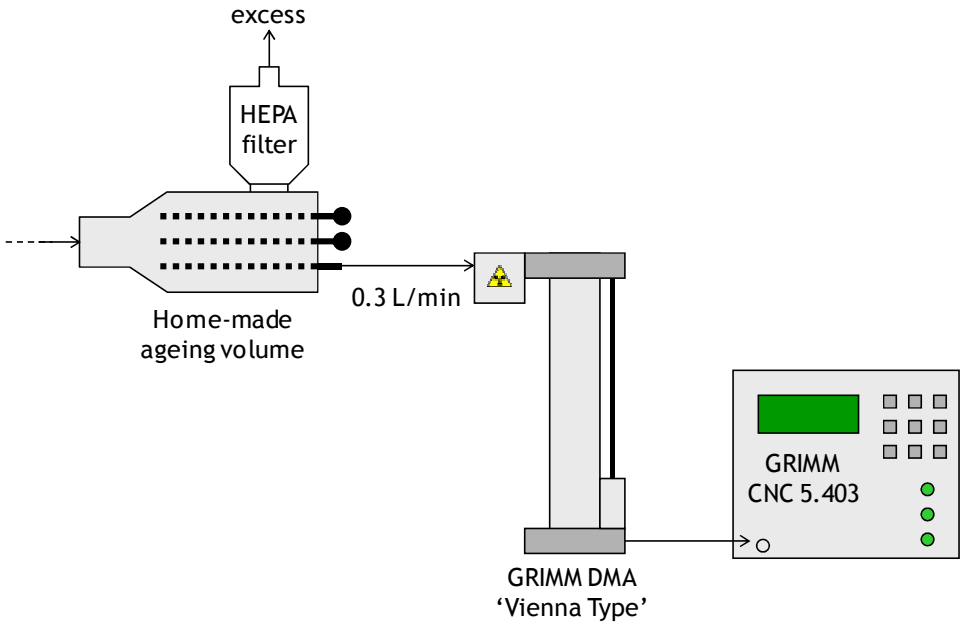

Figure 5: Set-up for the measurement of the number size distributions

In the following figures, error bars correspond to one standard deviation observed on a minimum of three SMPS scans. Furthermore, for each electrode material, a table summarizes the main characteristics of the aerosols produced, based on the SMPS measurements[5].

[5] In some cases where a part of the number size distribution of NP was not measured (out of range due to very small sizes), the total number concentration is underestimated.

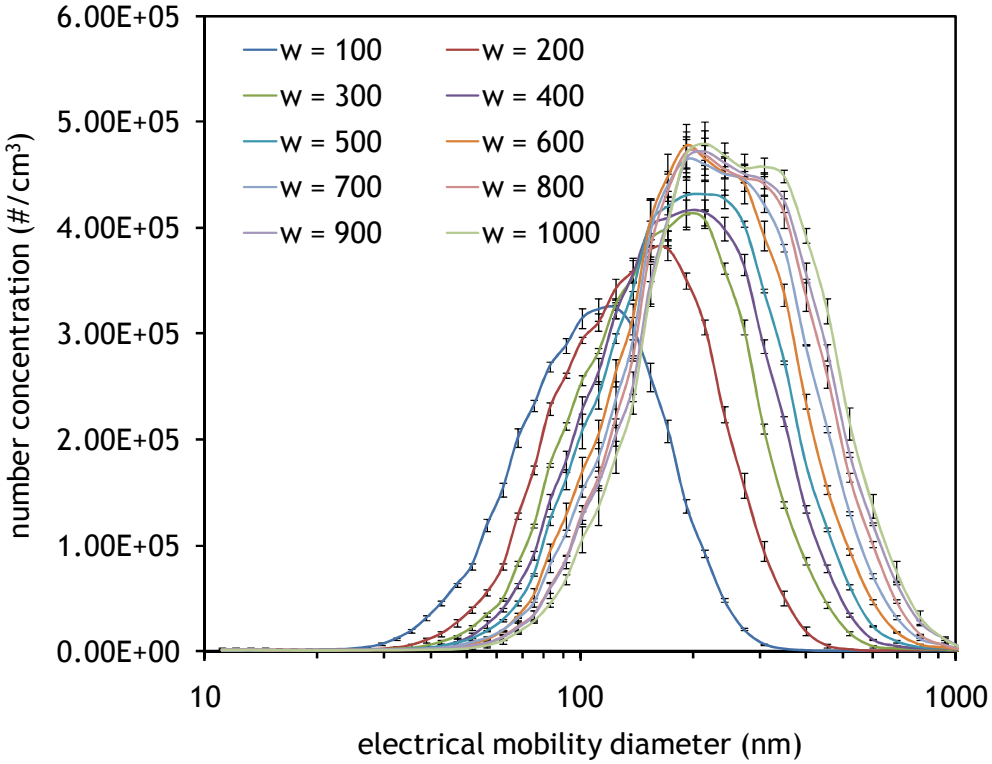

Figure 6: Effect of spark frequency ω on number-size distribution measured by SMPS for Carbon electrodes in configuration 1

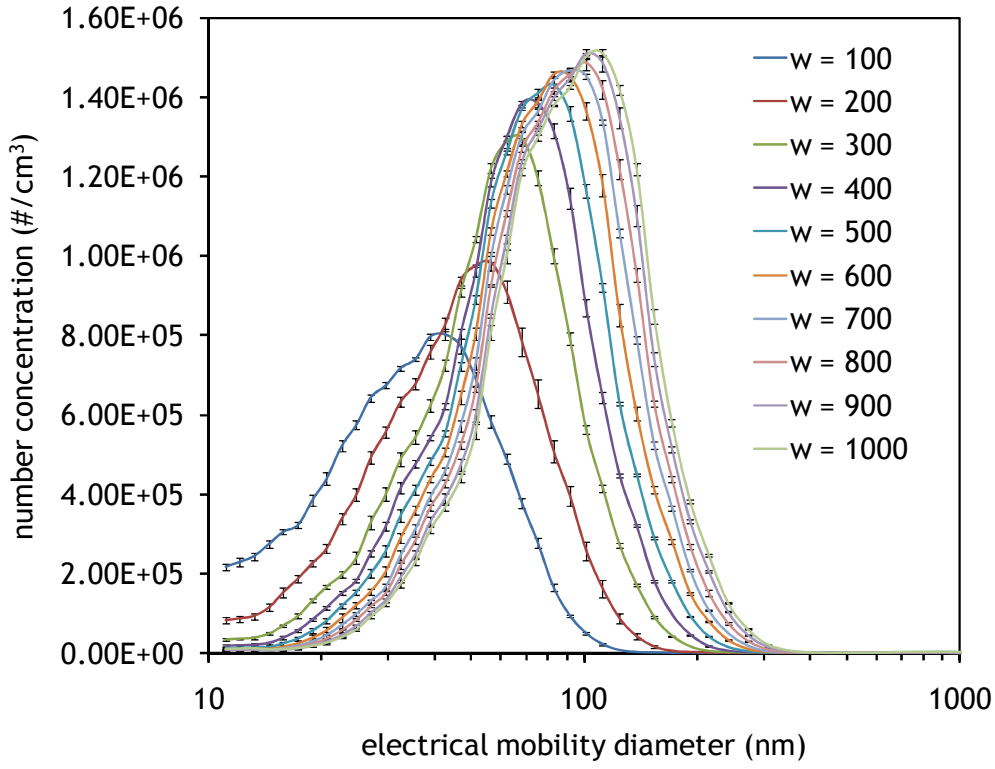

Figure 7: Effect of spark frequency ω on number-size distribution measured by SMPS for Carbon electrodes in configuration 2

Table 4: Properties of the number size distributions of Carbon-based NP aerosols versus spark-discharge frequency indication for the configuration 1 and 2

ω (a.u.)	configuration	C_N total (#/cm^3)	CMMD (nm)	σ_g (-)	Flux of particles (#/min)
100	1	$3.58 \cdot 10^6$	99	1.55	$4.48 \cdot 10^{10}$
200	1	$4.32 \cdot 10^6$	131	1.60	$5.40 \cdot 10^{10}$
300	1	$4.75 \cdot 10^6$	154	1.64	$5.94 \cdot 10^{10}$
400	1	$4.93 \cdot 10^6$	167	1.65	$6.16 \cdot 10^{10}$
500	1	$5.11 \cdot 10^6$	178	1.66	$6.39 \cdot 10^{10}$
600	1	$5.30 \cdot 10^6$	191	1.64	$6.63 \cdot 10^{10}$
700	1	$5.41 \cdot 10^6$	202	1.66	$6.76 \cdot 10^{10}$
800	1	$5.49 \cdot 10^6$	212	1.66	$6.86 \cdot 10^{10}$
900	1	$5.52 \cdot 10^6$	219	1.68	$6.90 \cdot 10^{10}$
1000	1	$5.56 \cdot 10^6$	228	1.67	$6.95 \cdot 10^{10}$
100	2	$1.14 \cdot 10^7$	33	1.72	$3.71 \cdot 10^{11}$
200	2	$1.26 \cdot 10^7$	44	1.67	$4.10 \cdot 10^{11}$
300	2	$1.45 \cdot 10^7$	56	1.60	$4.71 \cdot 10^{11}$
400	2	$1.55 \cdot 10^7$	63	1.59	$5.04 \cdot 10^{11}$
500	2	$1.62 \cdot 10^7$	68	1.57	$5.27 \cdot 10^{11}$
600	2	$1.67 \cdot 10^7$	73	1.57	$5.43 \cdot 10^{11}$
700	2	$1.70 \cdot 10^7$	77	1.57	$5.53 \cdot 10^{11}$
800	2	$1.72 \cdot 10^7$	80	1.57	$5.59 \cdot 10^{11}$
900	2	$1.74 \cdot 10^7$	84	1.57	$5.66 \cdot 10^{11}$
1000	2	$1.76 \cdot 10^7$	86	1.58	$5.72 \cdot 10^{11}$

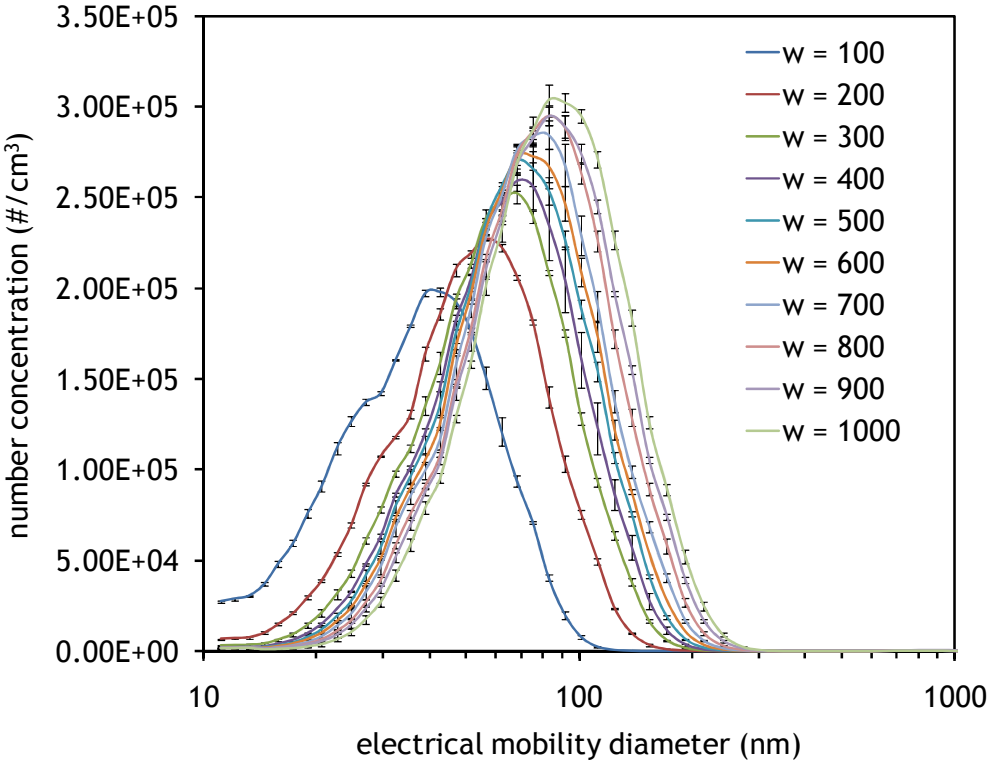

Figure 8: Effect of spark frequency ω on number-size distribution measured by SMPS for Aluminum electrodes in configuration 1

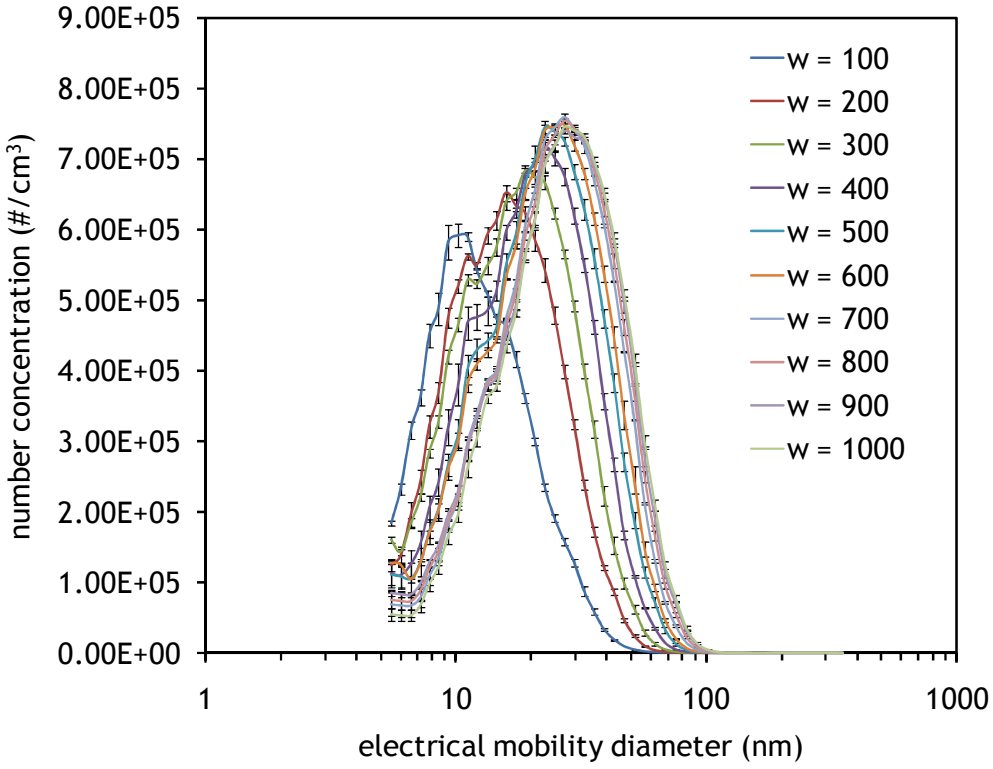

Figure 9: Effect of spark frequency ω on number-size distribution measured by SMPS for Aluminum electrodes in configuration 2

Table 5: Properties of the number size distributions of Aluminum-based NP aerosols versus spark-discharge frequency indication for the configuration 1 and 2

(a.u.)	configuration	C_N total (#/cm^3)	CMMD (nm)	σ_g (-)	Flux of particles (#/min)
100	1	$2.53 \cdot 10^6$	36	1.63	$3.16 \cdot 10^{10}$
200	1	$2.73 \cdot 10^6$	49	1.60	$3.41 \cdot 10^{10}$6.83
300	1	$2.90 \cdot 10^6$	57	1.57	$3.63 \cdot 10^{10}$7.25
400	1	$2.96 \cdot 10^6$	61	1.56	$3.70 \cdot 10^{10}$7.41
500	1	$3.09 \cdot 10^6$	64	1.57	$3.86 \cdot 10^{10}$7.72
600	1	$3.71 \cdot 10^6$	66	1.59	$4.64 \cdot 10^{10}$9.27
700	1	$3.24 \cdot 10^6$	68	1.56	$4.05 \cdot 10^{10}$8.09
800	1	$3.35 \cdot 10^6$	72	1.56	$4.19 \cdot 10^{10}$
900	1	$3.43 \cdot 10^6$	75	1.58	$4.29 \cdot 10^{10}$
1000	1	$3.72 \cdot 10^6$	78	1.57	$4.65 \cdot 10^{10}$
100	2	$7.79 \cdot 10^6$	11	1.60	$2.53 \cdot 10^{11}$
200	2	$9.65 \cdot 10^6$	15	1.67	$3.13 \cdot 10^{11}$
300	2	$1.07 \cdot 10^7$	17	1.73	$3.48 \cdot 10^{11}$
400	2	$1.09 \cdot 10^7$	19	1.73	$3.54 \cdot 10^{11}$
500	2	$1.13 \cdot 10^7$	21	1.76	$3.67 \cdot 10^{11}$
600	2	$1.17 \cdot 10^7$	21	1.79	$3.80 \cdot 10^{11}$
700	2	$1.13 \cdot 10^7$	24	1.74	$3.67 \cdot 10^{11}$
800	2	$1.16 \cdot 10^7$	24	1.77	$3.77 \cdot 10^{11}$
900	2	$1.17 \cdot 10^7$	24	1.80	$3.80 \cdot 10^{11}$
1000	2	$1.14 \cdot 10^7$	25	1.76	$3.71 \cdot 10^{11}$

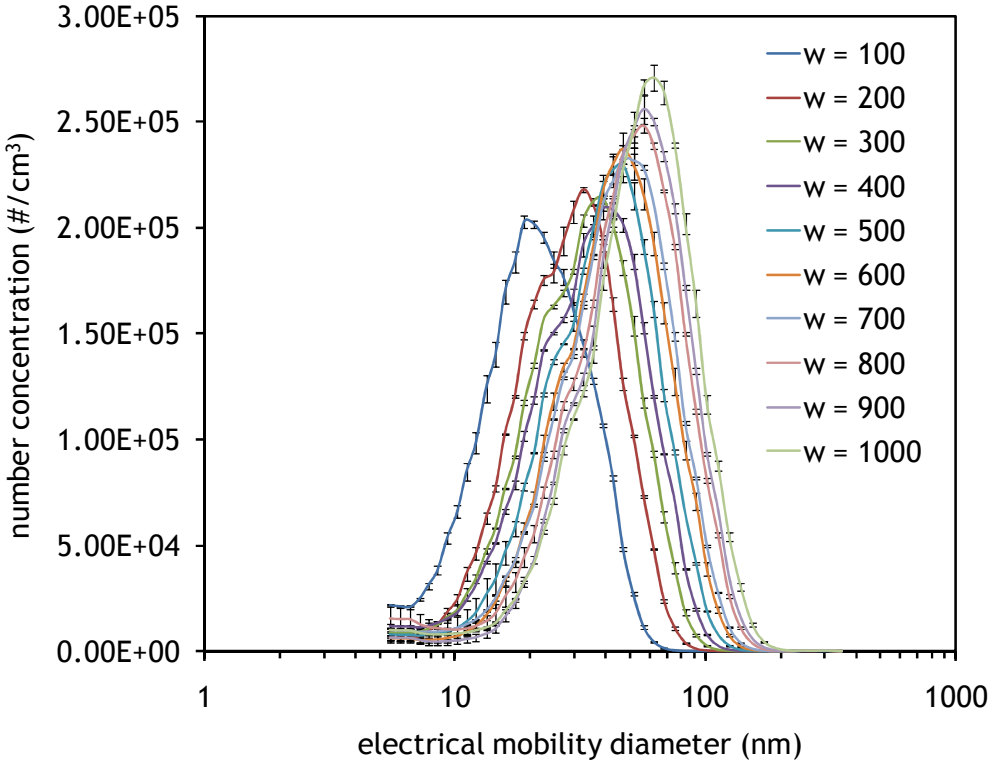

Figure 10: Effect of spark frequency ω on number-size distribution measured by SMPS for Copper electrodes in configuration 1

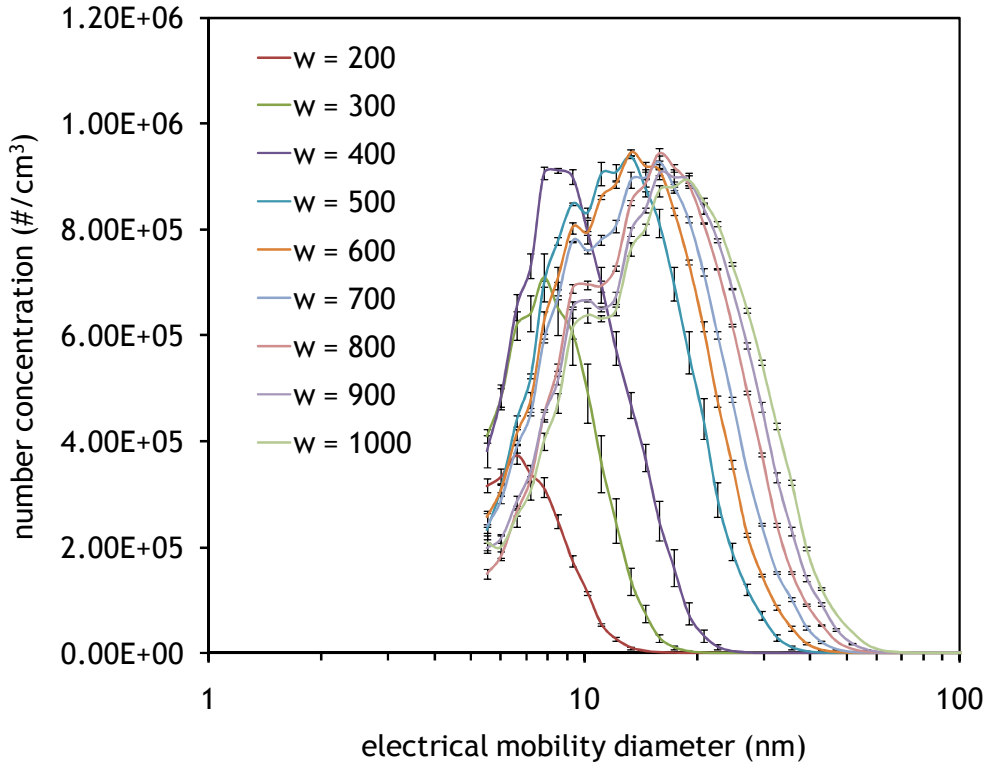

Figure 11: Effect of spark frequency ω on number-size distribution measured by SMPS for Copper electrodes in configuration 2

Table 6: Properties of the number size distributions of Copper-based NP aerosols versus spark-discharge frequency indication for the configuration 1 and 2

ω (a.u.)	configuration	C_N total (#/cm^3)	CMMD (nm)	σ_g (-)	Flux of particles (#/min)
100	1	$2.75 \cdot 10^6$	20	1.64	$3.44 \cdot 10^{10}$
200	1	$2.78 \cdot 10^6$	27	1.68	$3.48 \cdot 10^{10}$
300	1	$2.86 \cdot 10^6$	31	1.74	$3.58 \cdot 10^{10}$
400	1	$2.94 \cdot 10^6$	33	1.80	$3.68 \cdot 10^{10}$
500	1	$2.97 \cdot 10^6$	37	1.76	$3.71 \cdot 10^{10}$
600	1	$3.01 \cdot 10^6$	41	1.72	$3.76 \cdot 10^{10}$
700	1	$3.12 \cdot 10^6$	42	1.78	$3.90 \cdot 10^{10}$
800	1	$3.26 \cdot 10^6$	46	1.81	$4.08 \cdot 10^{10}$
900	1	$3.18 \cdot 10^6$	49	1.73	$3.98 \cdot 10^{10}$
1000	1	$3.39 \cdot 10^6$	52	1.79	$4.24 \cdot 10^{10}$
100	2	Not measured			
200	2	$2.31 \cdot 10^6$	7	1.26	$7.51 \cdot 10^{10}$
300	2	$5.48 \cdot 10^6$	8	1.32	$1.78 \cdot 10^{11}$
400	2	$8.41 \cdot 10^6$	9	1.38	$2.73 \cdot 10^{11}$
500	2	$1.15 \cdot 10^7$	11	1.51	$3.74 \cdot 10^{11}$
600	2	$1.25 \cdot 10^7$	12	1.57	$4.06 \cdot 10^{11}$
700	2	$1.29 \cdot 10^7$	13	1.62	$4.19 \cdot 10^{11}$
800	2	$1.28 \cdot 10^7$	14	1.62	$4.16 \cdot 10^{11}$
900	2	$1.32 \cdot 10^7$	15	1.68	$4.29 \cdot 10^{11}$
1000	2	$1.34 \cdot 10^7$	16	1.70	$4.36 \cdot 10^{11}$

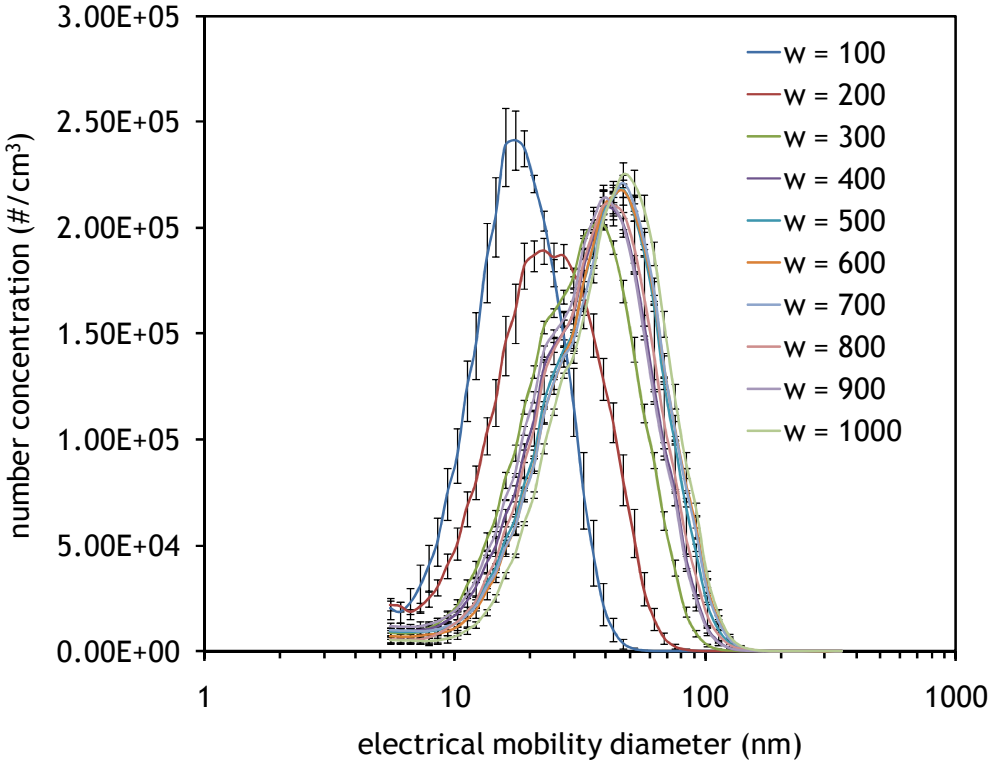

Figure 12: Effect of spark frequency ω on number-size distribution measured by SMPS for Silver electrodes in configuration 1

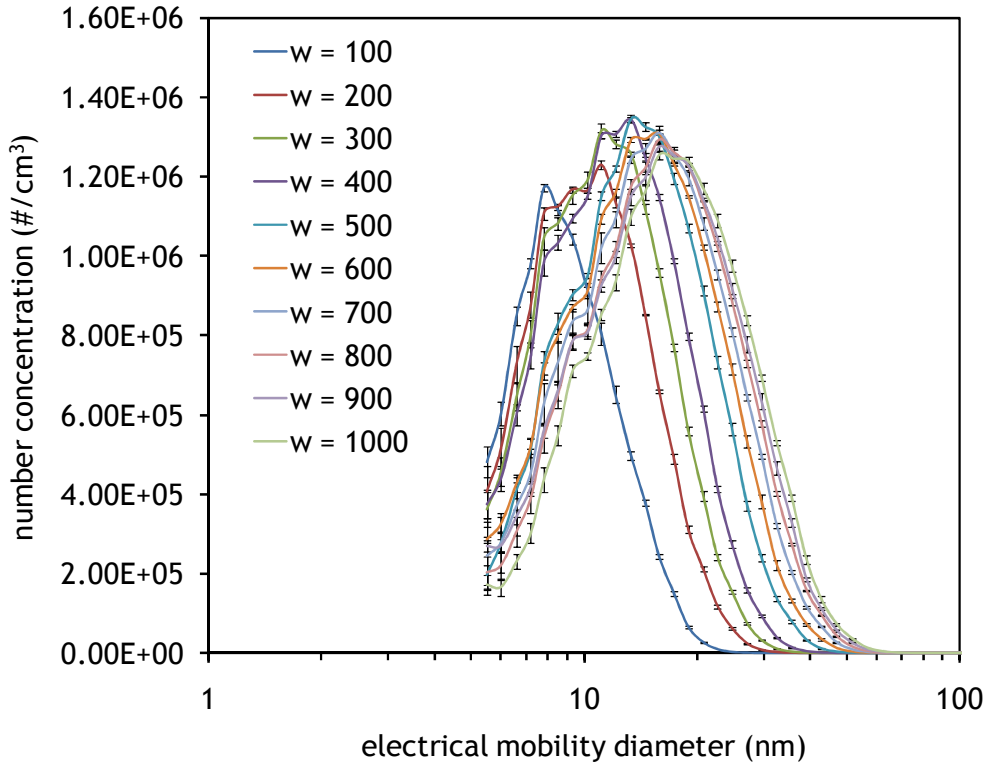

Figure 13: Effect of spark frequency ω on number-size distribution measured by SMPS for Silver electrodes in configuration 2

Table 7: Properties of the number size distributions of Silver-based NP aerosols versus spark-discharge frequency indication for the configuration 1 and 2

ω (a.u.)	configuration	C_N total (#/cm^3)	CMMD (nm)	σ_g (-)	Flux of particles (#/min)
100	1	$2.75 \cdot 10^6$	17	1.51	$3.44 \cdot 10^{10}$
200	1	$2.75 \cdot 10^6$	22	1.67	$3.44 \cdot 10^{10}$
300	1	$2.80 \cdot 10^6$	30	1.67	$3.50 \cdot 10^{10}$
400	1	$2.89 \cdot 10^6$	34	1.70	$3.61 \cdot 10^{10}$
500	1	$2.96 \cdot 10^6$	37	1.70	$3.70 \cdot 10^{10}$
600	1	$2.97 \cdot 10^6$	38	1.69	$3.71 \cdot 10^{10}$
700	1	$2.97 \cdot 10^6$	38	1.70	$3.71 \cdot 10^{10}$
800	1	$2.90 \cdot 10^6$	35	1.68	$3.63 \cdot 10^{10}$
900	1	$2.99 \cdot 10^6$	35	1.72	$3.74 \cdot 10^{10}$
1000	1	$2.90 \cdot 10^6$	41	1.65	$3.63 \cdot 10^{10}$
100	2	$9.99 \cdot 10^6$	8	1.36	$3.25 \cdot 10^{11}$
200	2	$1.32 \cdot 10^7$	10	1.44	$4.29 \cdot 10^{11}$
300	2	$1.49 \cdot 10^7$	11	1.47	$4.84 \cdot 10^{11}$
400	2	$1.62 \cdot 10^7$	11	1.52	$5.27 \cdot 10^{11}$
500	2	$1.65 \cdot 10^7$	13	1.55	$5.36 \cdot 10^{11}$
600	2	$1.74 \cdot 10^7$	14	1.60	$5.66 \cdot 10^{11}$
700	2	$1.75 \cdot 10^7$	14	1.62	$5.69 \cdot 10^{11}$
800	2	$1.74 \cdot 10^7$	15	1.62	$5.66 \cdot 10^{11}$
900	2	$1.78 \cdot 10^7$	15	1.66	$5.79 \cdot 10^{11}$
1000	2	$1.73 \cdot 10^7$	16	1.63	$5.62 \cdot 10^{11}$

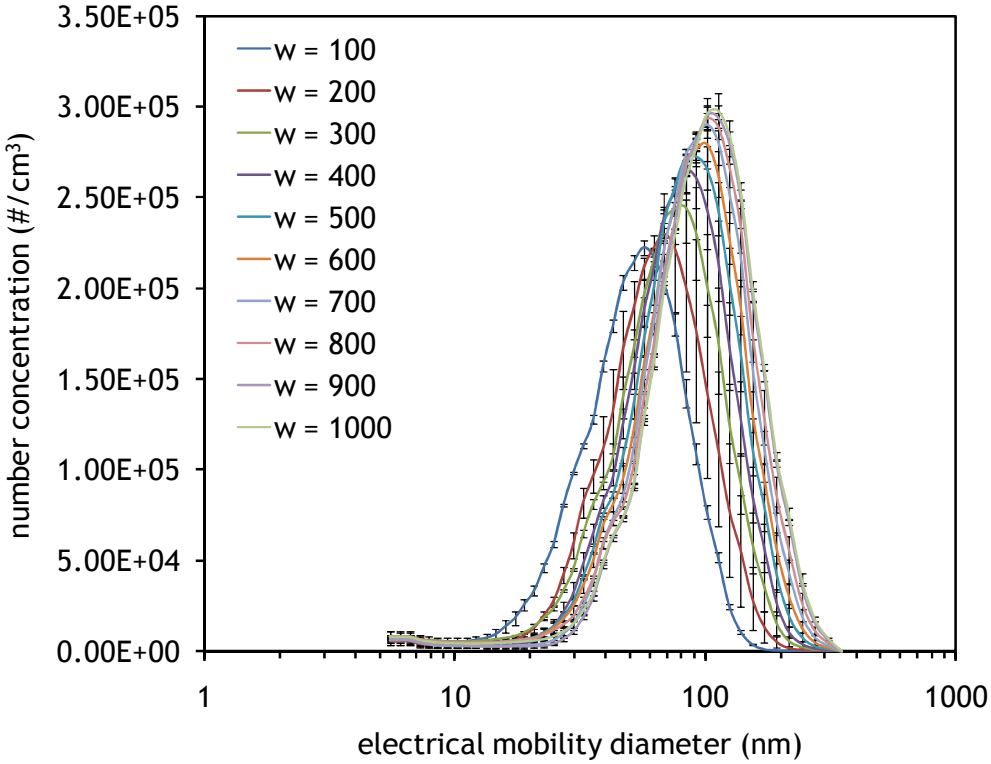

Figure 14: Effect of spark frequency ω on number-size distribution measured by SMPS for Constantane electrodes in configuration 1

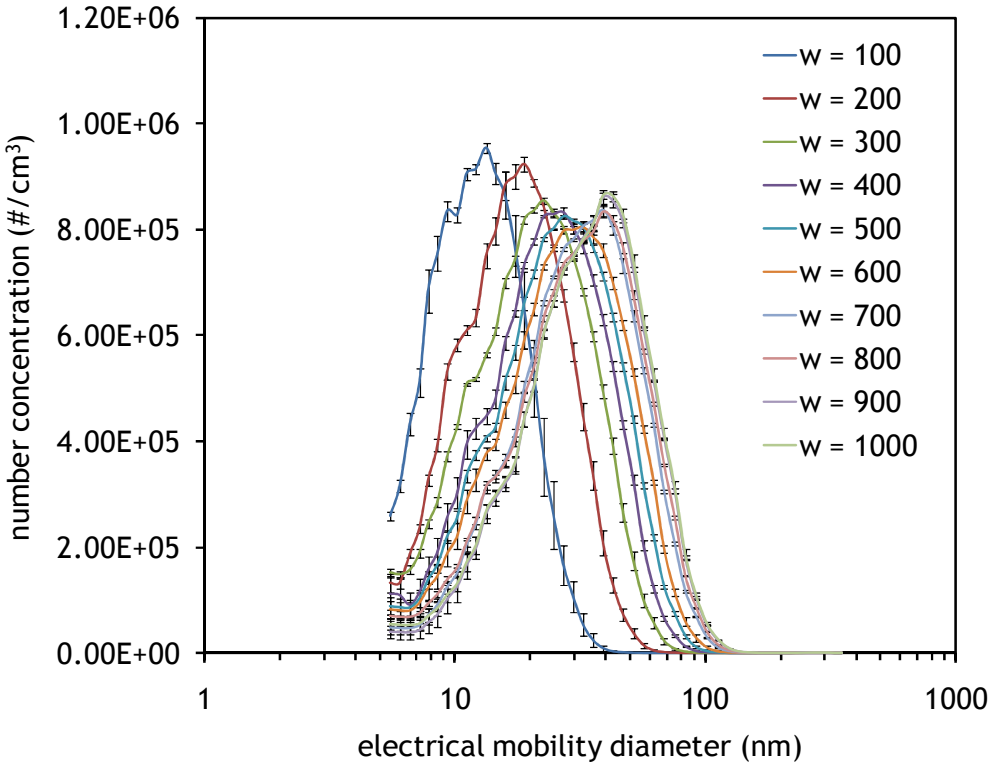

Figure 15: Effect of spark frequency ω on number-size distribution measured by SMPS for Constantane electrodes in configuration 2

Table 8: Properties of the number size distributions of Constantane-based NP aerosols versus spark-discharge frequency indication for the configuration 1 and 2

ω (a.u.)	configuration	C_N total (#/cm^3)	CMMD (nm)	σ_g (-)	Flux of particles (#/min)
100	1	$2.69 \cdot 10^6$	49	1.61	$3.36 \cdot 10^{10}$
200	1	$2.71 \cdot 10^6$	60	1.59	$3.39 \cdot 10^{10}$
300	1	$2.96 \cdot 10^6$	67	1.64	$3.70 \cdot 10^{10}$
400	1	$3.08 \cdot 10^6$	73	1.59	$3.85 \cdot 10^{10}$
500	1	$3.22 \cdot 10^6$	78	1.61	$4.03 \cdot 10^{10}$
600	1	$3.26 \cdot 10^6$	81	1.61	$4.08 \cdot 10^{10}$
700	1	$3.30 \cdot 10^6$	86	1.58	$4.13 \cdot 10^{10}$
800	1	$3.41 \cdot 10^6$	88	1.62	$4.26 \cdot 10^{10}$
900	1	$3.38 \cdot 10^6$	92	1.58	$4.23 \cdot 10^{10}$
1000	1	$2.59 \cdot 10^6$	92	1.61	$3.24 \cdot 10^{10}$
100	2	$1.21 \cdot 10^7$	12	1.54	$3.93 \cdot 10^{11}$
200	2	$1.30 \cdot 10^7$	16	1.66	$4.23 \cdot 10^{11}$
300	2	$1.33 \cdot 10^7$	19	1.77	$4.32 \cdot 10^{11}$
400	2	$1.30 \cdot 10^7$	22	1.77	$4.23 \cdot 10^{11}$
500	2	$1.31 \cdot 10^7$	24	1.79	$4.26 \cdot 10^{11}$
600	2	$1.31 \cdot 10^7$	26	1.81	$4.26 \cdot 10^{11}$
700	2	$1.28 \cdot 10^7$	29	1.77	$4.16 \cdot 10^{11}$
800	2	$1.31 \cdot 10^7$	30	1.83	$4.26 \cdot 10^{11}$
900	2	$1.29 \cdot 10^7$	32	1.76	$4.19 \cdot 10^{11}$
1000	2	$1.31 \cdot 10^7$	32	1.79	$4.26 \cdot 10^{11}$

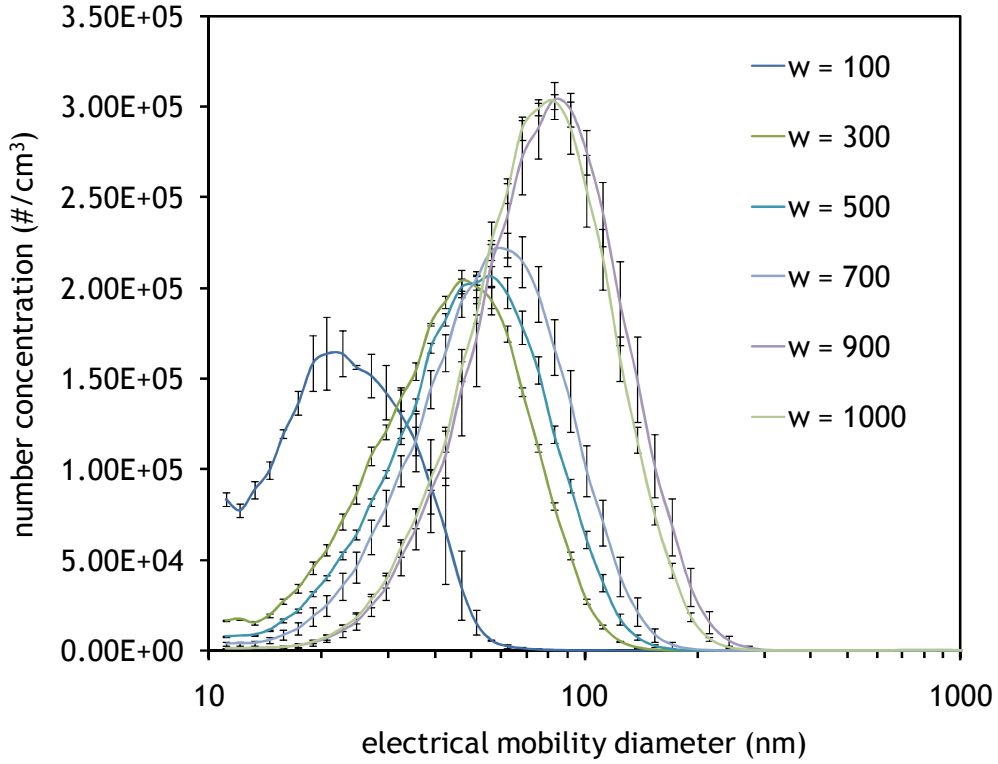

Figure 16: Effect of spark frequency ω on number-size distribution measured by SMPS for Cu/Be electrodes in configuration 1

Table 9: Properties of the number size distributions of Cu/Be-based NP aerosols versus spark-discharge frequency indication for the configuration 1

ω (a.u.)	configuration	C_N total (#/cm³)	CMMD (nm)	σ_g (-)	Flux of particles (#/min)
100	1	$2.01 \cdot 10^6$	22	1.52	$2.51 \cdot 10^{10}$
300	1	$1.87 \cdot 10^6$	42	1.60	$2.34 \cdot 10^{10}$
500	1	$2.53 \cdot 10^6$	47	1.59	$3.16 \cdot 10^{10}$
700	1	$2.63 \cdot 10^6$	53	1.58	$3.29 \cdot 10^{10}$
900	1	$3.43 \cdot 10^6$	74	1.57	$4.29 \cdot 10^{10}$
1000	1	$3.35 \cdot 10^6$	71	1.55	$4.19 \cdot 10^{10}$

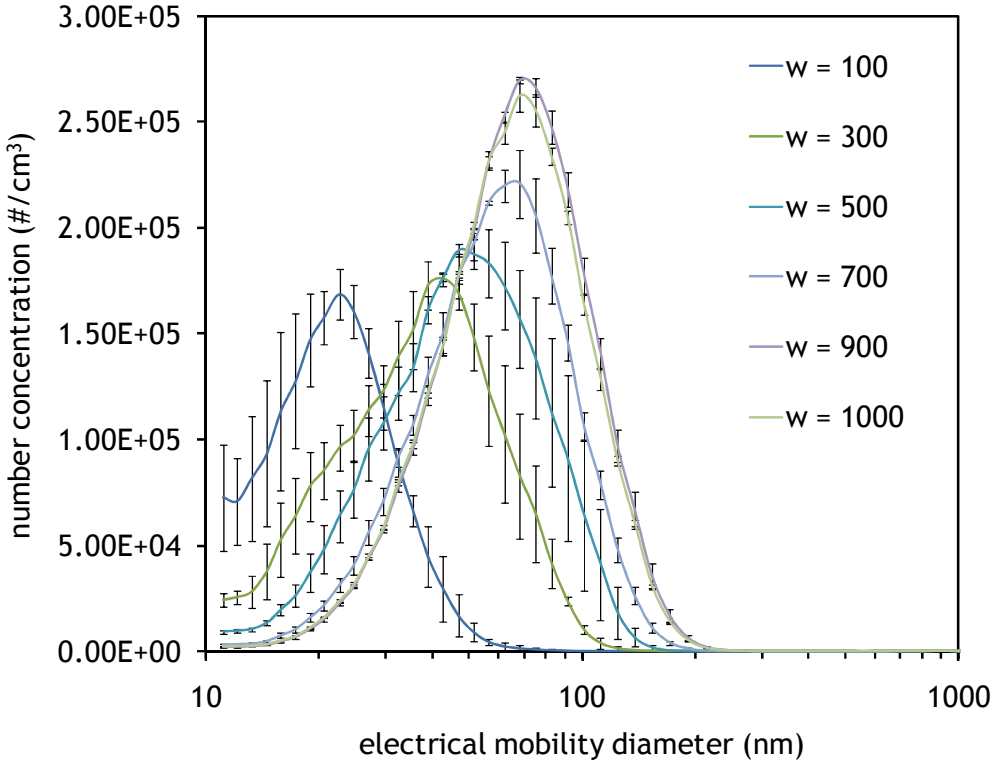

Figure 17: Effect of spark frequency ω on number-size distribution measured by SMPS for Cu/Co/Be electrodes in configuration 1

Table 10: Properties of the number size distributions of Cu/Co/Be-based NP aerosols versus spark-discharge frequency indication for the configuration 1

ω (a.u.)	configuration	C_N total (#/cm^3)	CMMD (nm)	σ_g (-)	Flux of particles (#/min)
100	1	$1.71 \cdot 10^6$	21	1.45	$2.14 \cdot 10^{10}$
300	1	$1.79 \cdot 10^6$	36	1.67	$2.24 \cdot 10^{10}$
500	1	$2.48 \cdot 10^6$	45	1.65	$3.10 \cdot 10^{10}$
700	1	$2.58 \cdot 10^6$	55	1.57	$3.23 \cdot 10^{10}$
900	1	$3.04 \cdot 10^6$	63	1.57	$3.80 \cdot 10^{10}$
1000	1	$2.96 \cdot 10^6$	61	1.57	$3.70 \cdot 10^{10}$

It can be observed from Figure 11 and Figure 13 that the aerosols generated are bimodal, with a first population around 9 nm, corresponding to primary particle size.

In the case of Carbon-based NP (Figure 6), bimodal aerosols are also found for sparking frequencies above 600 a.u. The first mode, situated around 200 nm, remains quite stable, while the second one keeps on increasing (250 nm to 300 nm) with spark discharge frequency.

Figure 18 and Figure 19 present the count median mobility diameters (CMMD) for all types of electrode as a function of the spark-discharge frequency for configurations 1 and 2 respectively.

It can be observed a significant evolution of the CMMD as a function of the spark frequency and additional air flow conditions imposed. In configuration 1, CMMD were found between 17 nm and 228 nm. In configuration 2, the range of CMMD extends from 7 to 87 nm. This decrease in particle size can be linked to lower coagulation effects by (1) dilution due to additional 20 L/min air flow rate, and (2) decrease of residence time (by a factor of 9).

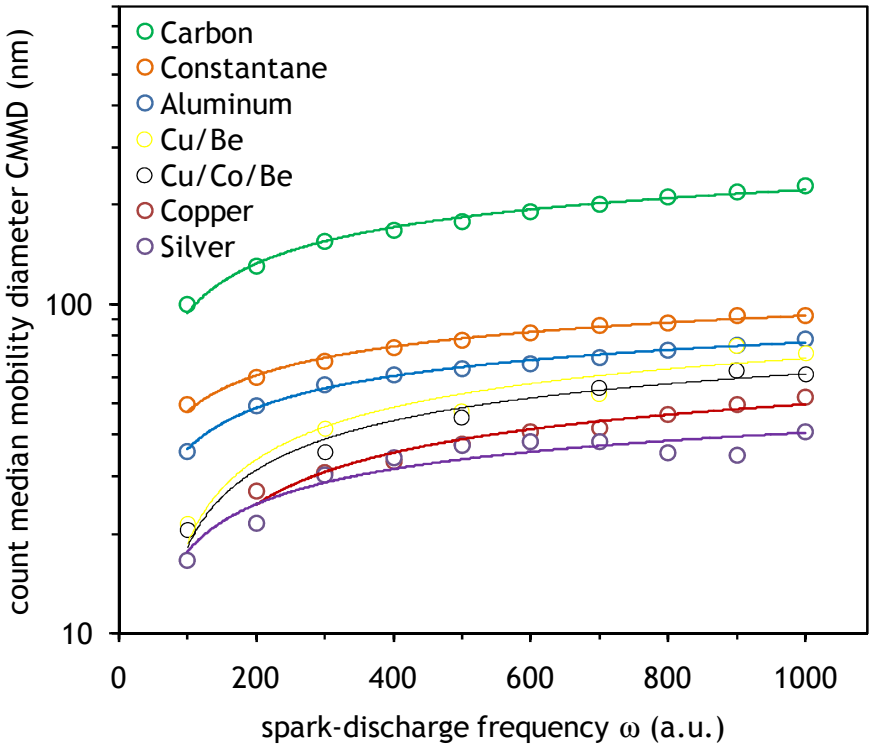

Figure 18: Airborne NP count median mobility diameter for the different materials in configuration 1

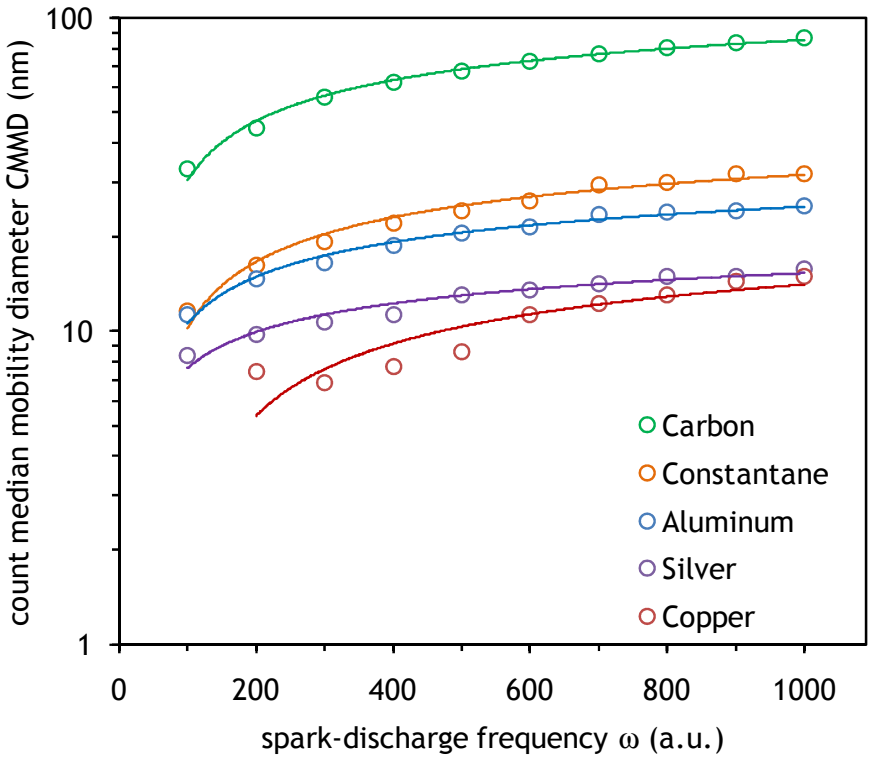

Figure 19: Airborne NP count median mobility diameter for the different materials in configuration 2

Figure 20 show TEM micrographs of Carbon, Aluminum, Copper and Silver-based NP sampled within the ageing volume of the CAIMAN setup. Airborne NP were collected mainly by diffusion on copper TEM-grids (200 mesh with a carbon film) taped onto a 25 mm diameter PVC filter (0.08-µm pore size) and placed on a backup filter. Air flow was driven from the ageing volume to the sampling cassette at a regulated flow rate of 2 L/min. All NP were collected in configuration 1 with ω = 1000 a.u. during 5 to 20 minutes depending on the aerosol total concentration.

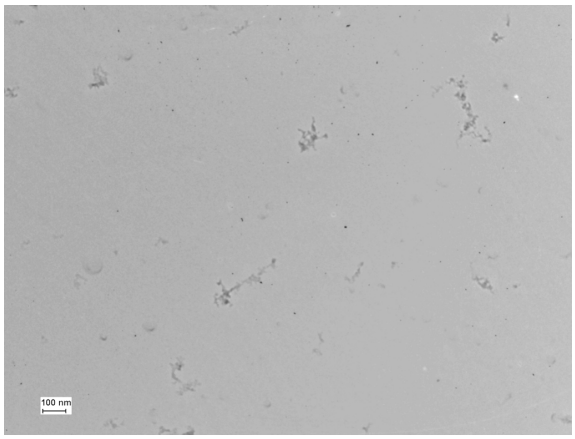

Carbon

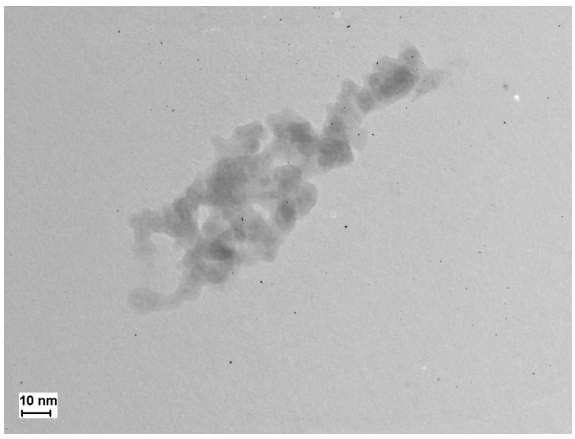

Aluminum

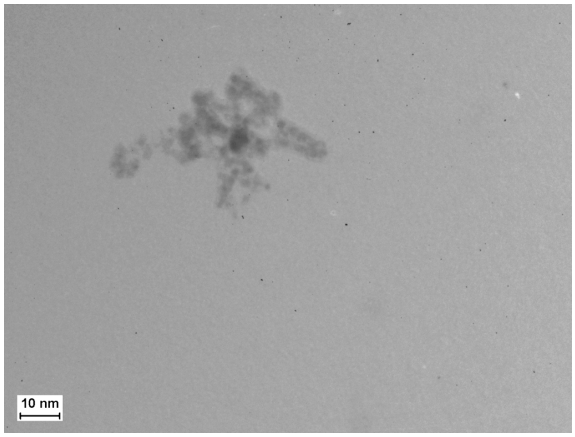

Copper

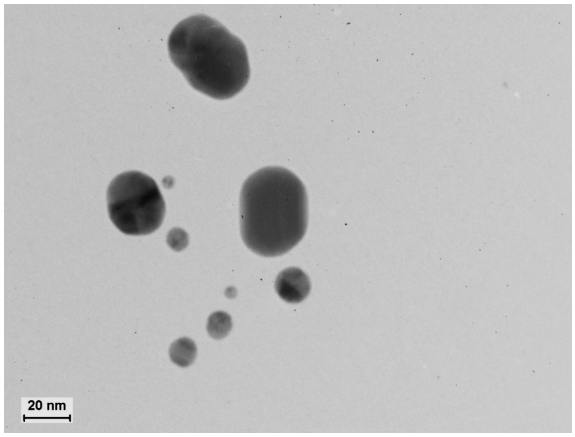

Silver

Figure 20: TEM picture of sampled airborne NP in configuration 1 with ω = 1000 a.u. (continued)

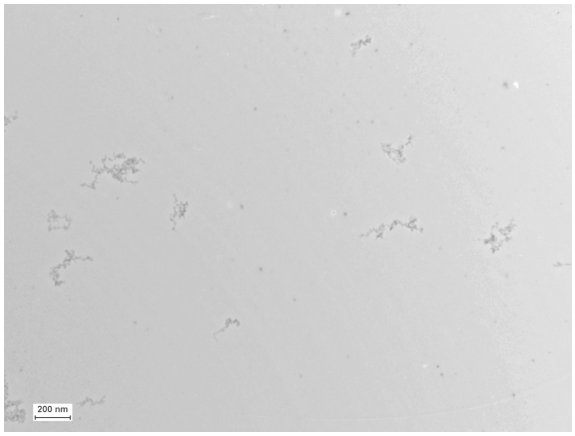

Constantane

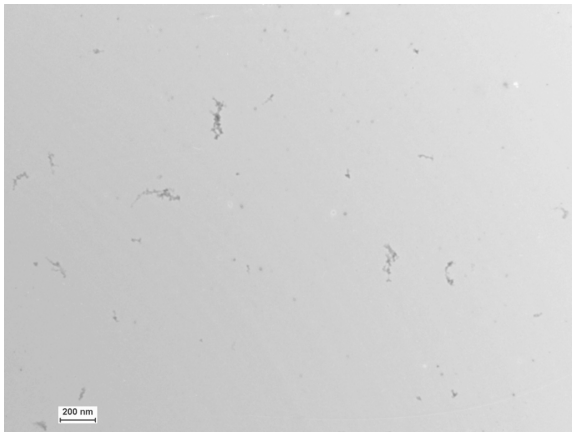

Cu/Be

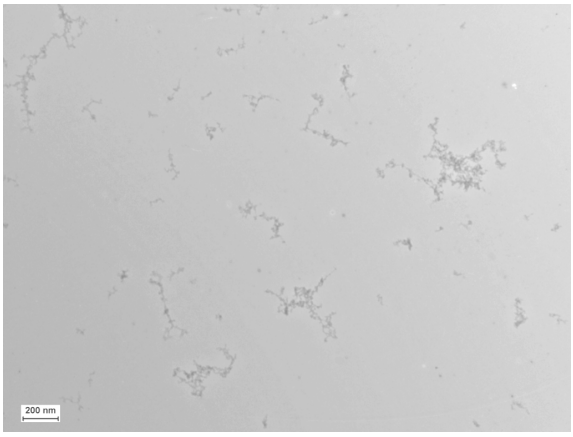

Cu/Co/Be

Figure 20 : TEM picture of sampled airborne NP in configuration 1 with ω = 1000 a.u. (concluded)

From these TEM micrographs, it can be seen that all collected NP are aggregates, except those stemming from Silver which are spherical. This might be due to the non oxidation of Silver-based NP, which enables primary particles to coalesce in absence of an oxidation layer, leading to metal-metal contacts, as stated by Tabrizi *et al*. [11].

Furthermore, collected NP were measured on TEM pictures, leading to the mean sizes indicated in Table 11.

Table 11: Mean size of collected NP in configuration 1 with ω = 1000 a.u.

Electrode	mean size (nm) ± standard deviation (nm)
C	102 ± 60
Al	171 ± 129
Cu	95 ± 47
Ag	25 ± 14
Constantane	243 ± 149
Cu/Be	135 ± 71
Cu/Co/Be	241 ± 162

Interestingly, the mean size measured on the TEM pictures is very different than the one obtained from SMPS measurements. Furthermore, it is found that the mean size of Constantane-, Cu/Co/Be-, Cu/Be- and Al-based particles is above the one measured for C-based NP.

However, it should be kept in mind that the particle diameter given in SMPS is the equivalent electrical mobility diameter. In the case of aggregates, which are neither spherical nor compact, this equivalent diameter can be very different from the real physical particle size.

3.3. Mass concentrations

No mass measurements were performed during this qualification campaign. However, a previous study carried out on another CAIMAN configuration allowed this determination by means of a TEOM system. If the data cannot be directly used because of configuration modification of CAIMAN, Table 12 presents the range of mass concentrations of airborne NP produced and maximum mass production rate.

Table 12: Range of mass concentrations and mass rates of NP

Electrode	Range of mass concentration ($\mu g/m^3$)	Maximum mass rate ($\mu g/h$)
C	800 – 6400	4800
Al	< 20 – 450	340
Cu	< 20 – 240	180
Ag	< 20 - 680	510
Cu/Be	110 – 1800	1350
Cu/Co/Be	140 - 740	555

3.4. Electrical state-of-charge

The mean charge per airborne NP generated within our facility was determined by the simultaneous measurement of the number concentration (GRIMM CNC model 5.403) and current (electrometer TSI model 3068B). The mean charge per particle ($\overline{p}$) is given by:

$$\overline{p} = \frac{I}{C_N \cdot e \cdot Q}$$

where C_N corresponds to the mean number concentration of airborne NP (measured by the CNC), I is the mean current (measured by the electrometer), e represents the elementary charge ($e = 1.602 \cdot 10^{-19}$ C) and Q is the flow rate of the electrometer (adjusted from 0.3 to 5 L/min to measure a current well above the limit of quantification of the electrometer).

Figure 21 is a schematic of the experimental set-up used for the measurement of the electrical state-of-charge of airborne NP produced within CAIMAN.

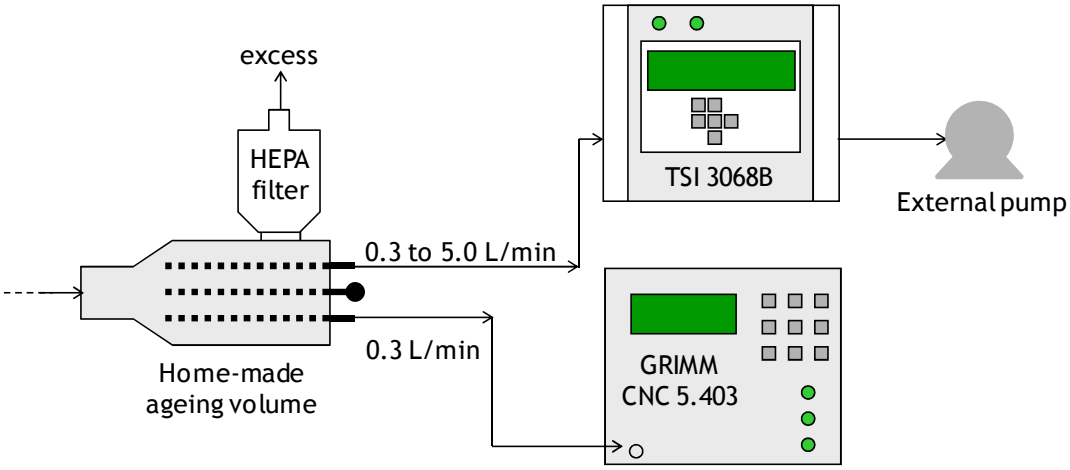

Figure 21: Set-up for the measurement of the mean state-of-charge of NP

Figures 29 to 38 present the mean charge per particle ($\overline{p}$) as a function of spark-discharge frequency for three conditions:

- Additional positive ions
- Additional negative ions
- No addition of ions (raw mean charge per particle).

Ion addition was performed by ionizing a fixed flow rate of 20 L/min of HEPA-filtered air within the bipolar ion generator (TOPAS EAN 581).

These experiments were not performed on wires containing Beryllium.

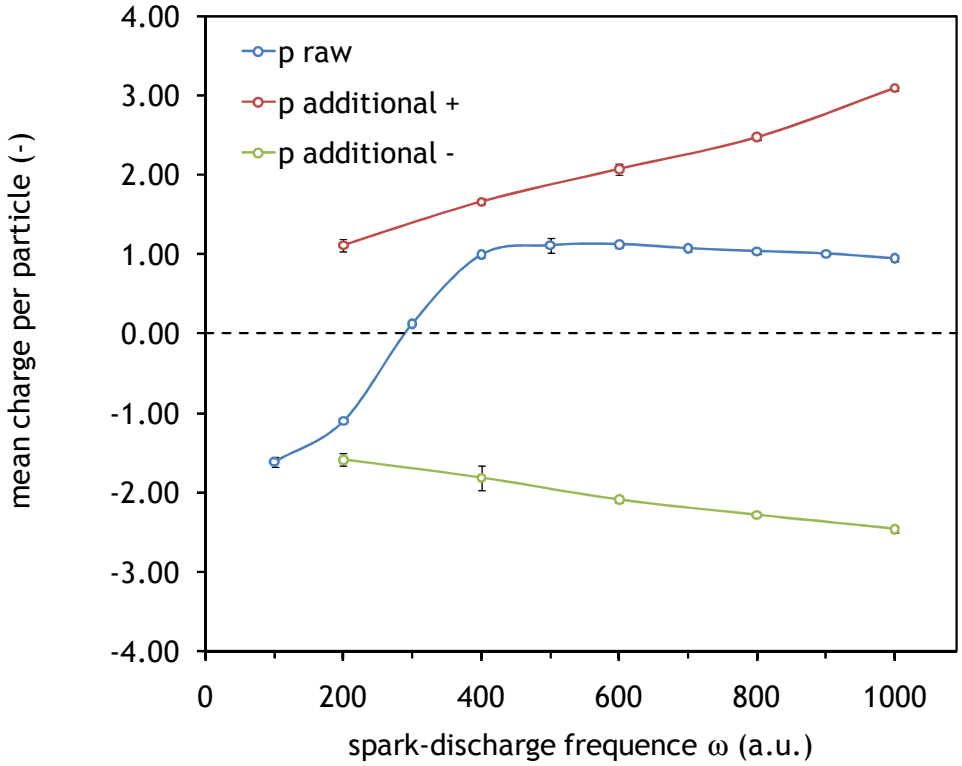

Figure 22: Airborne NP mean charge for Carbon electrodes in configuration 1

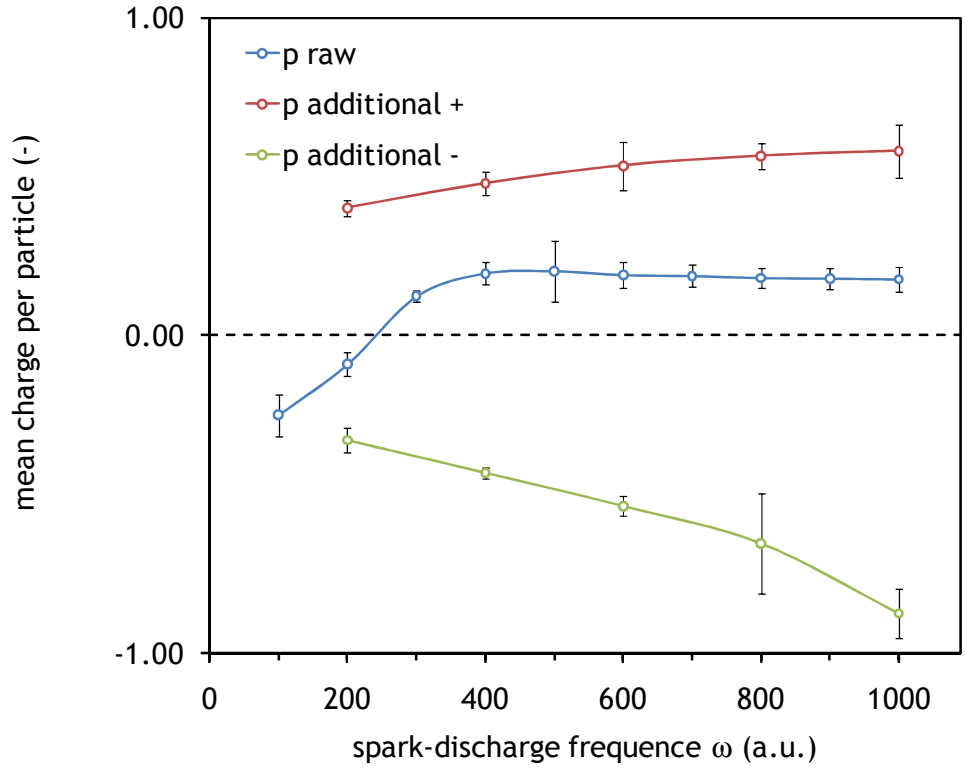

Figure 23: Airborne NP mean charge for Carbon electrodes in configuration 2

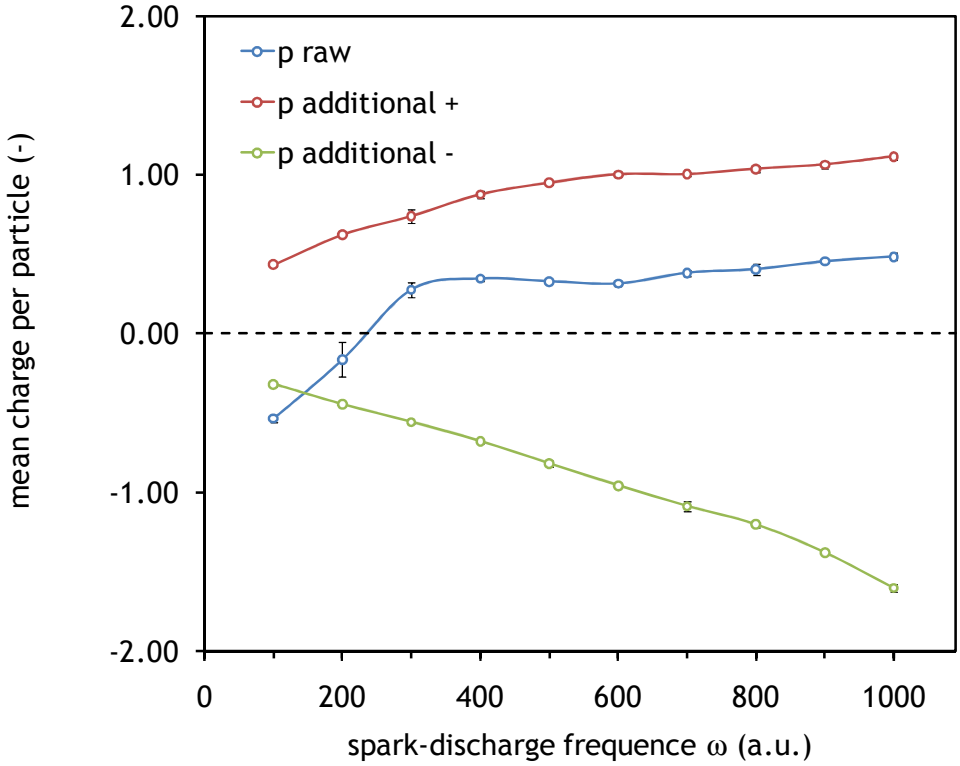

Figure 24: Airborne NP mean charge for Aluminum electrodes in configuration 1

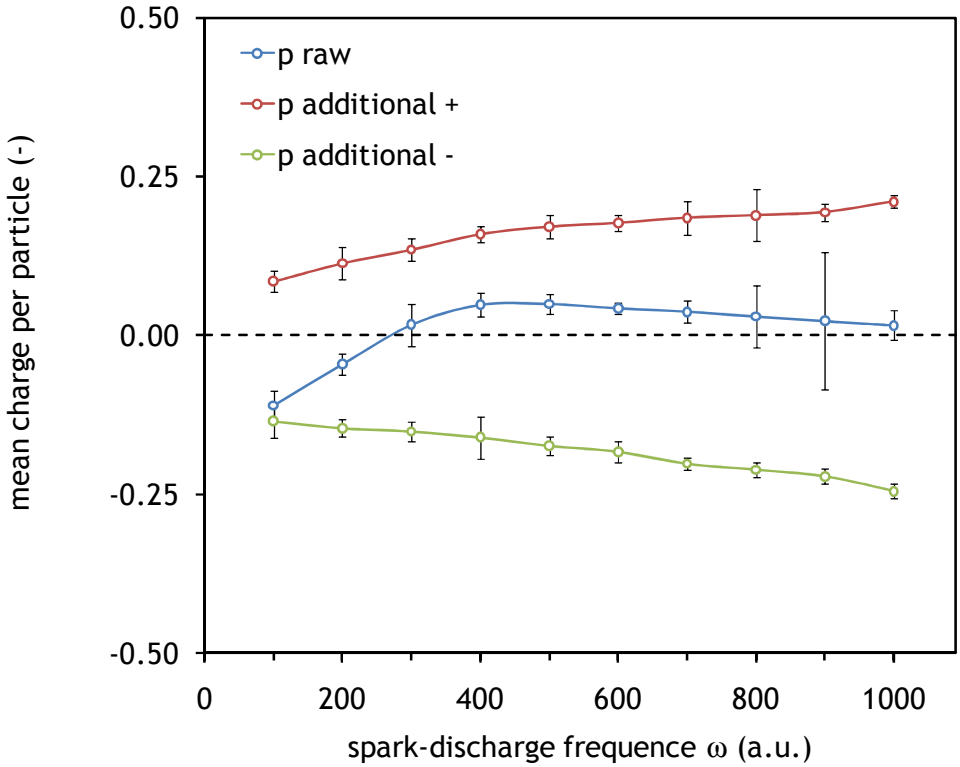

Figure 25: Airborne NP mean charge for Aluminum electrodes in configuration 2

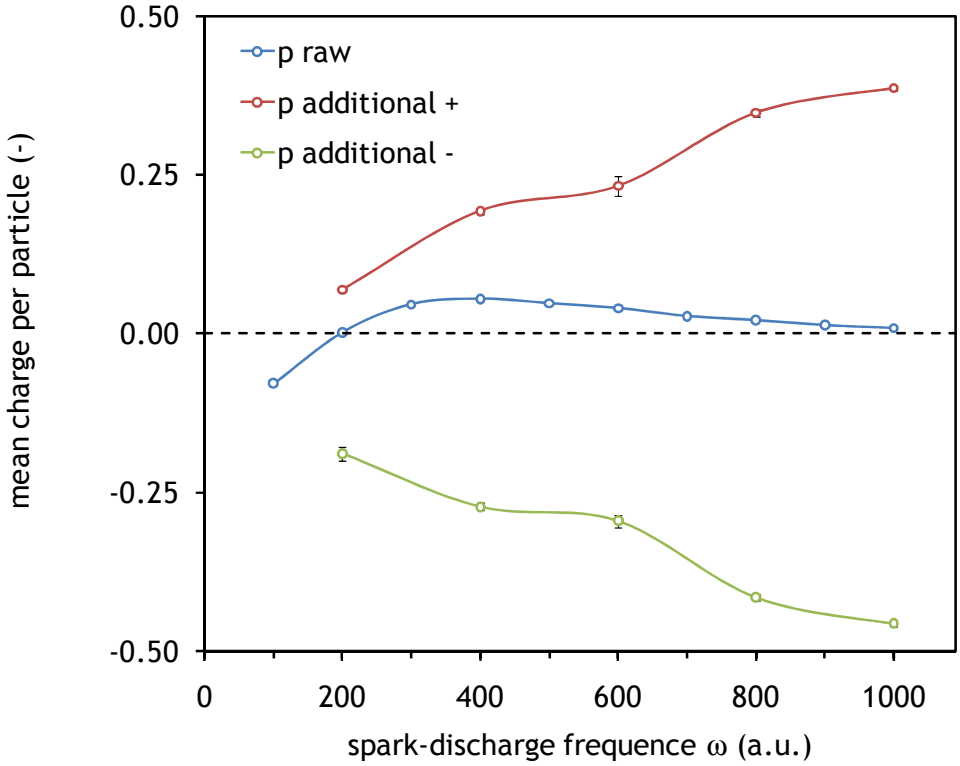

Figure 26: Airborne NP mean charge for Copper electrodes in configuration 1

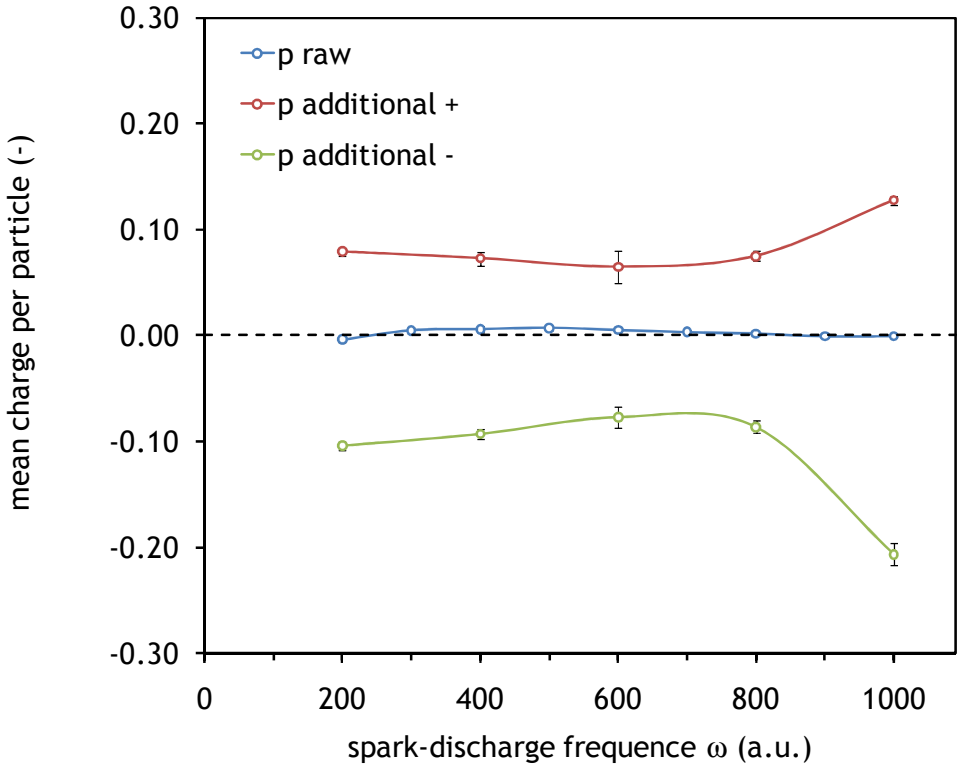

Figure 27: Airborne NP mean charge for Copper electrodes in configuration 2

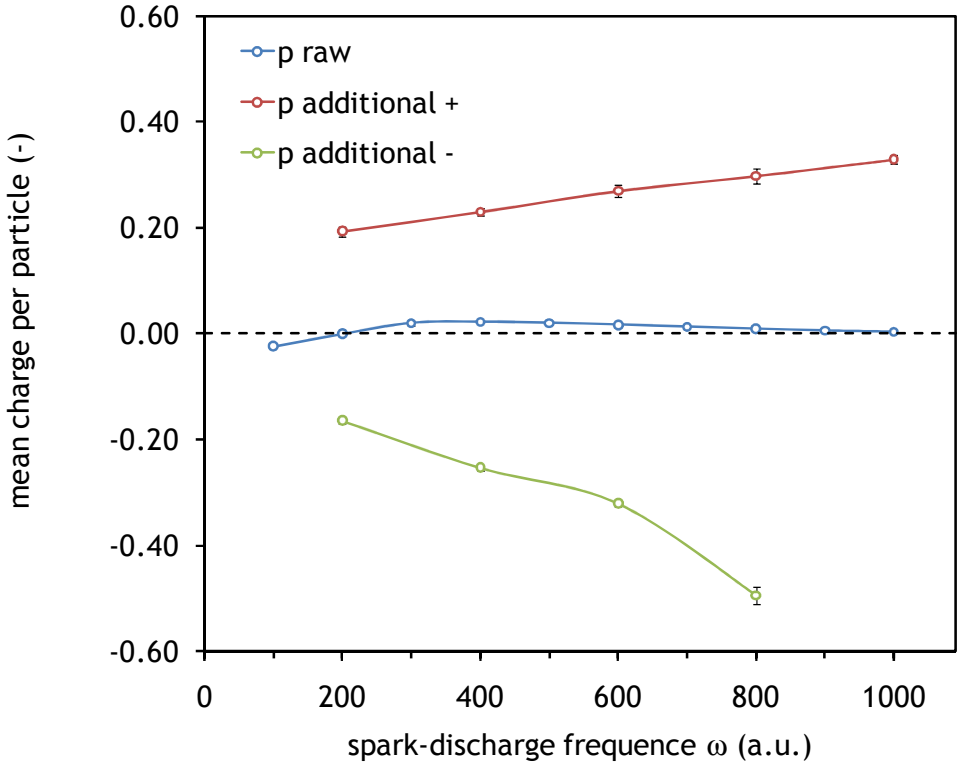

Figure 28: Airborne NP mean charge for Silver electrodes in configuration 1

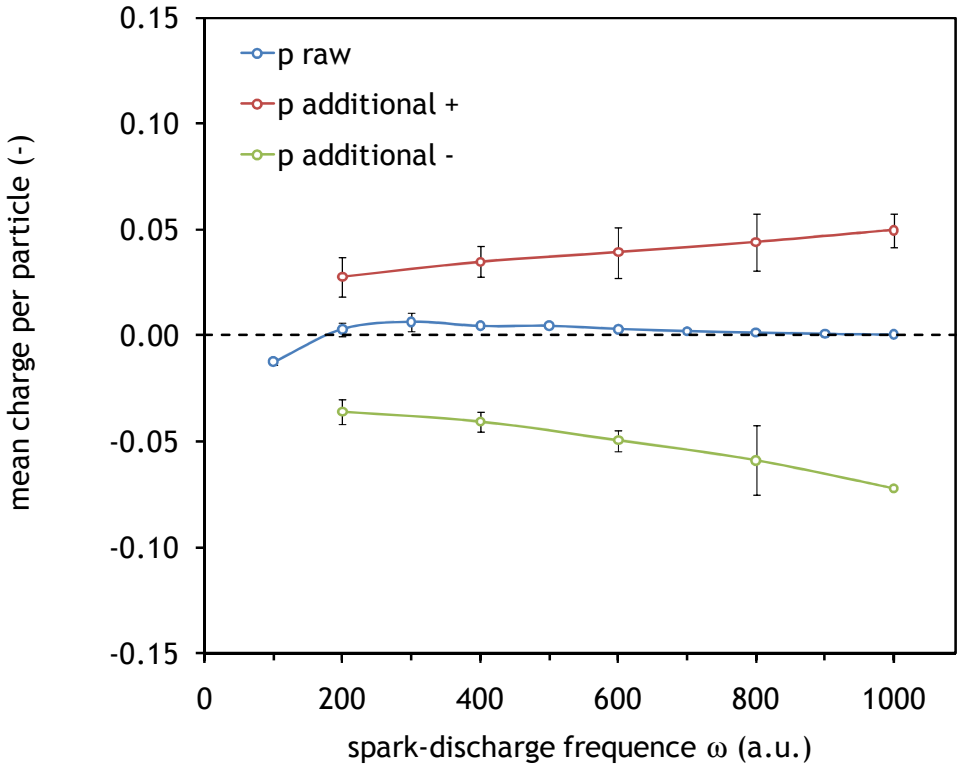

Figure 29: Airborne NP mean charge for Silver electrodes in configuration 2

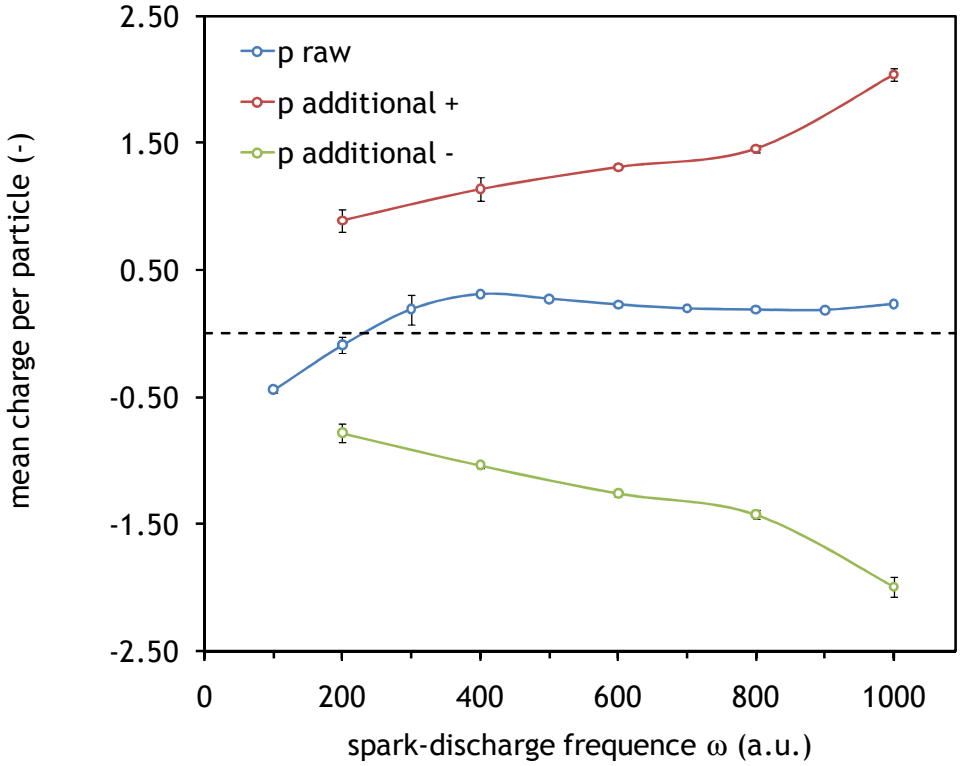

Figure 30: Airborne NP mean charge for Constantane electrodes in configuration 1

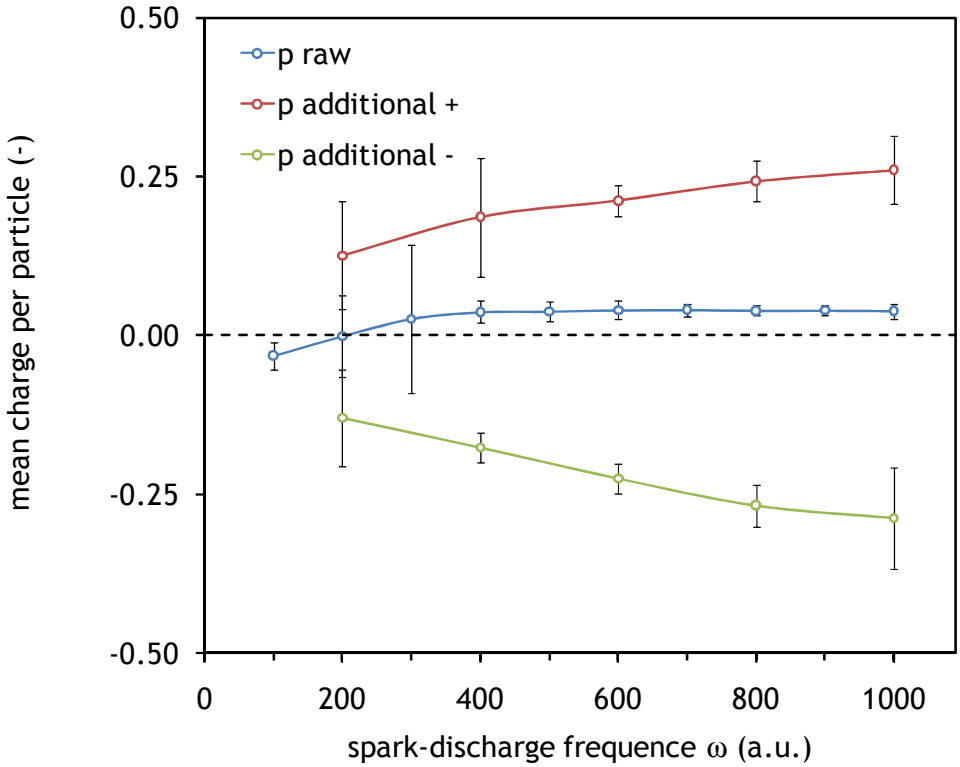

Figure 31: Airborne NP mean charge for Constantane electrodes in configuration 2

The same behavior can be noted for each electrode material. For sparking frequencies below 200-300 a.u., the raw mean charge per particle is negative, and becomes positive for sparking frequencies above this limit. The addition of ions produced within the ion generator lead to a wide range of possibilities in terms of electrical state-of-charge of airborne NP, summarized in Table 13.

Table 13: Range of variation of the mean charge per particle of airborne NP

Electrode material	Range of variation of						Configuration
	raw $\overline{p}$		$\overline{p}$ with $\oplus$ ions		$\overline{p}$ with $\ominus$ ions		
C	-1.61	0.94	1.11	3.09	-1.59	-2.46	1
	-0.25	0.18	0.40	0.58	-0.33	-0.88	2
Al	-0.53	0.48	0.43	1.11	-0.32	-1.60	1
	-0.11	0.05	0.09	0.21	-0.13	-0.24	2
Cu	-0.08	0.05	0.07	0.39	-0.19	-0.46	1
	0.00	0.01	0.06	0.13	-0.08	-0.21	2
Ag	-0.02	0.02	0.19	0.33	-0.16	-0.49	1
	-0.01	0.01	0.03	0.05	-0.04	-0.07	2
Constantane	-0.44	0.31	0.89	2.04	-0.78	-1.99	1
	-0.03	0.04	0.13	0.26	-0.13	-0.29	2

3.5. Particle shape

Partial sintering of primary particles constituting aggregates of Aluminum-based NP was observed by use of the high-temperature furnace. As a consequence, airborne NP morphology was varied from chain-like aggregates to “compact” aggregates when increasing the temperature within the furnace. In parallel of NP sampling, SMPS number size distributions were measured, as presented in Figure 32. Another representation of these distributions is proposed in Figure 33 in terms of cumulative distributions.

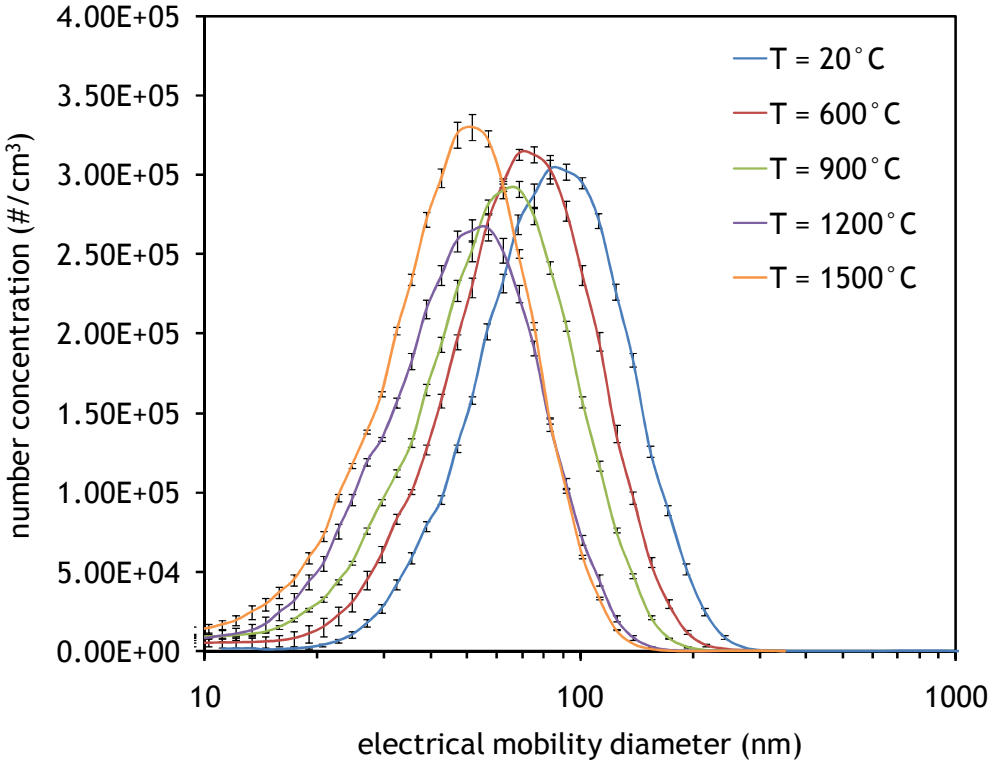

Figure 32: Effect of the furnace temperature on the number size distributions measured for Aluminum electrodes in configuration 1, ω = 1000 a.u.

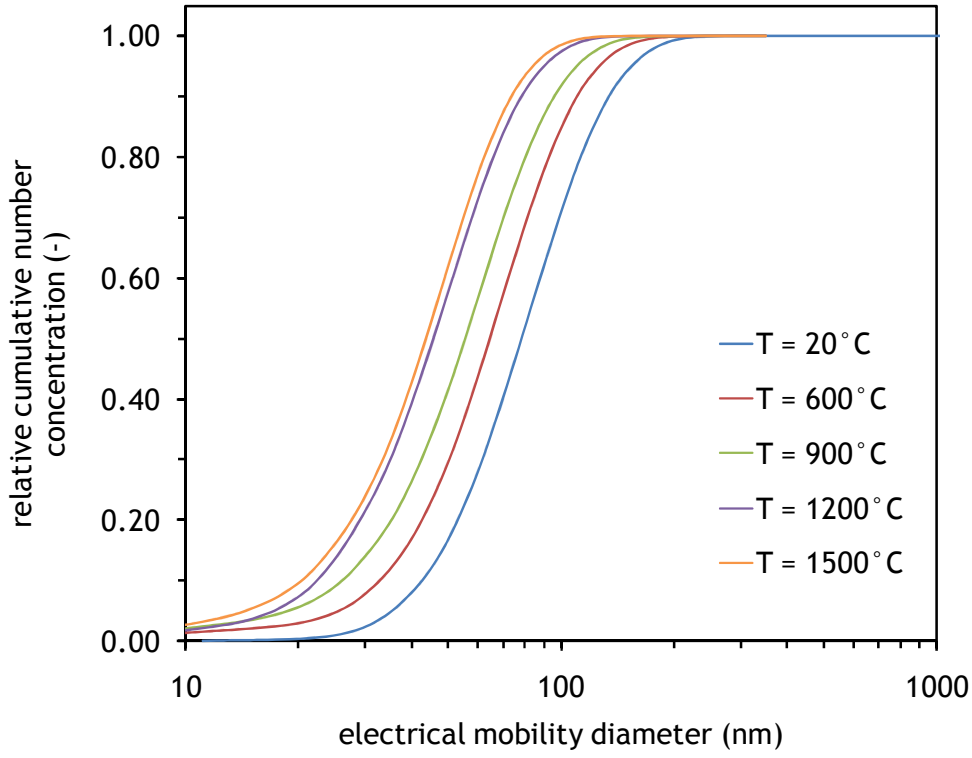

Figure 33: Effect of the furnace temperature on the cumulative number size distributions of airborne NP for Aluminum electrodes in configuration 1, ω = 1000 a.u.

From these figures, it can be observed that the number size distributions of airborne NP tend to smaller particles when temperature increases. Figure 34 shows the evolution of the CMMD of the aerosols with the temperature from 78 to 44 nm.

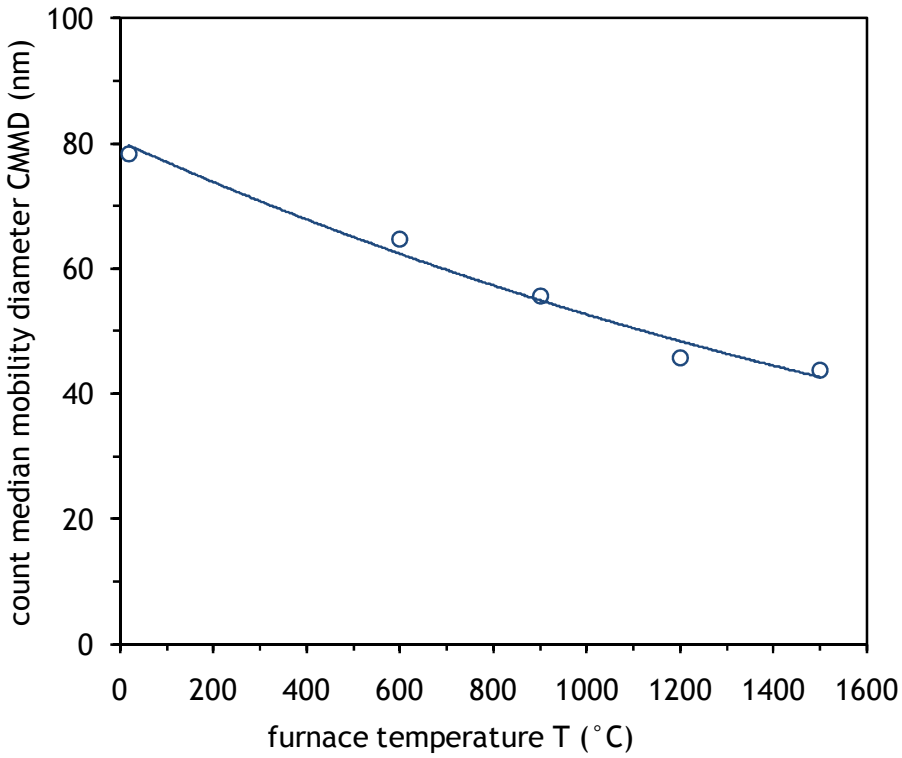

Figure 34: Effect of the furnace temperature on the airborne NP count median mobility diameter for Aluminum electrodes in configuration 1, ω = 1000 a.u.

In parallel, the mean size of Al-based NP was measured on different TEM micrographs. The same tendency is observed, since the collected NP mean size decreases by a factor of 3.5 from 171 nm at ambient temperature to 48 nm at 1500°C. Intermediate mean sizes are 107 nm at 900°C and 86 nm at 1200°C.

The residence time within the high-temperature furnace varied with temperature. During these tests, it was chosen to keep the flow rate constant through the furnace. This led to the following residence times:

- 13.8 seconds at ambient temperature,
- 7.0 seconds at 600°C,
- 5.5 seconds at 900°C,
- 4.6 seconds at 1200°C,
- 3.9 seconds at 1500°C.

Figure 35 presents TEM pictures of sampled Aluminum-based NP for the different temperatures. Particle restructuring can be highlighted in these pictures when increasing temperature.

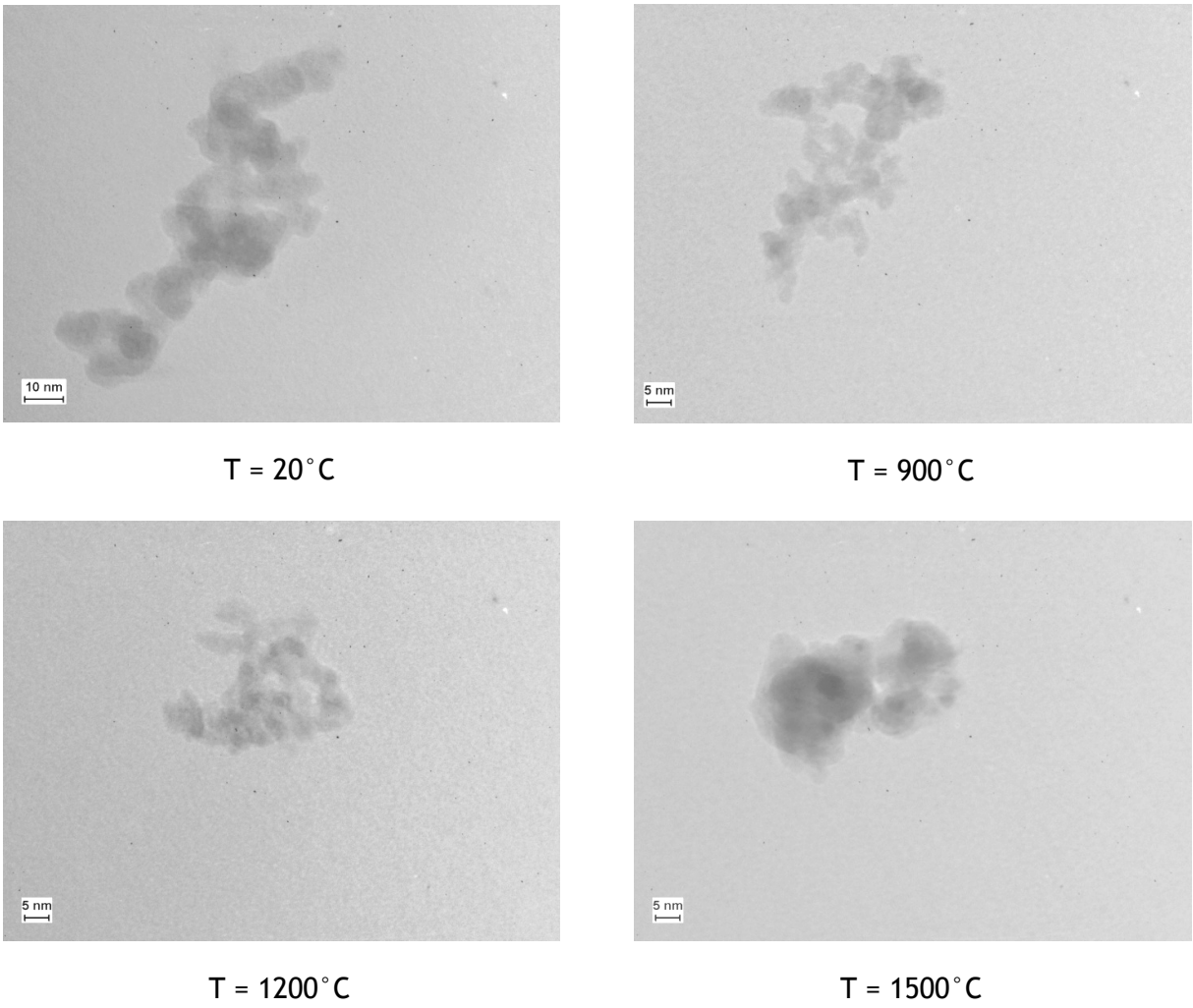

T = 20°C

T = 900°C

T = 1200°C

T = 1500°C

Figure 35: Change of morphologies for airborne NP for Aluminum electrodes at various sintering temperatures: ambient temperature (20°C), sintering at 900°C; sintering at 1200°C; sintering at 1500°C.

From Figure 35, it can be observed that particles tend to be more compact when temperature increases. This feature may be useful for studying the effect of particle morphology with constant chemistry on instruments behavior.

3.6. Aerosol dilution

To avoid saturating the instruments in study, airborne NP were produced in configurations 1 and 2 from Carbon electrodes with ω = 1000 a.u.

The additional air flow rate injected within the ageing volume (notated Q_5) was successively set to 10 (normal configuration), 20, 30, 40 and 50 L/min. The relative number size distributions measured by SMPS are presented in Figure 36 for configuration 1 and in Figure 37 for configuration 2.

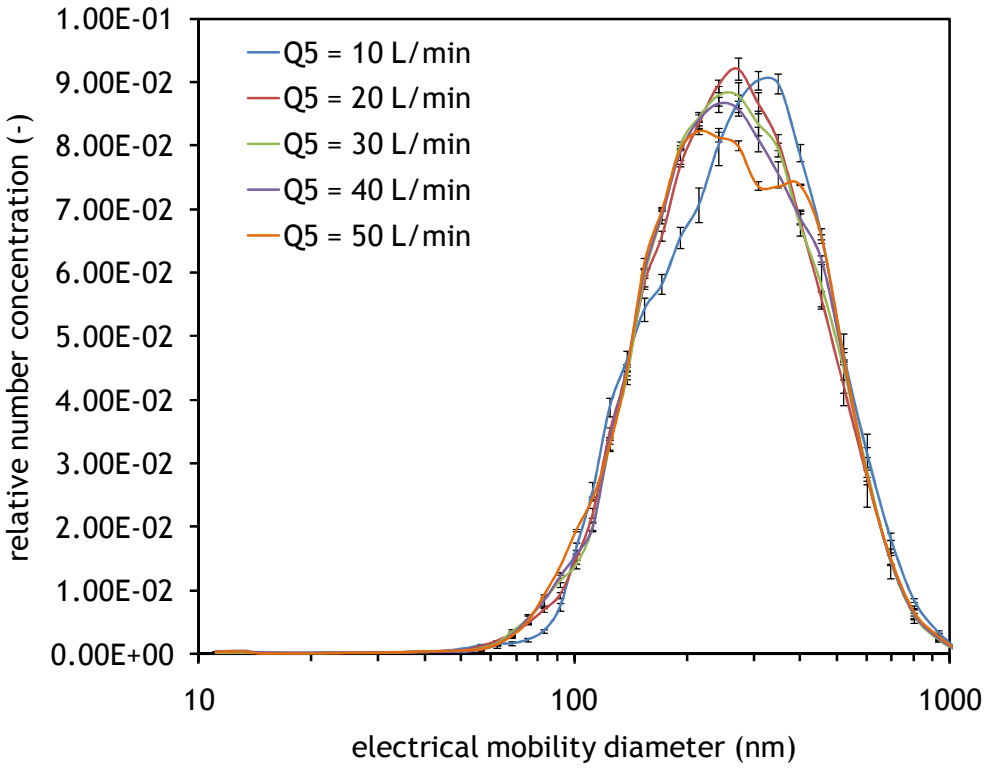

Figure 36: Effect of the dilution flow rate (Q_5) on the relative number size distributions measured for Carbon electrodes in configuration 1 with ω = 1000 a.u.

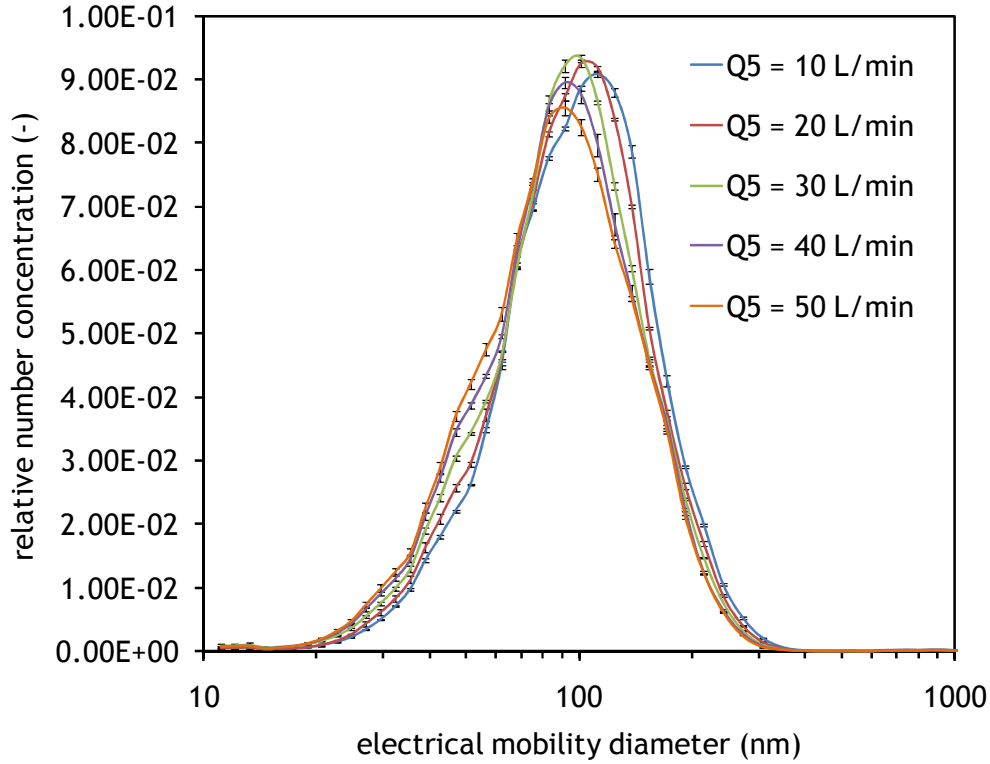

Figure 37: Effect of the dilution flow rate (Q_5) on the relative number size distributions measured for Carbon electrodes in configuration 2 with ω = 1000 a.u. and varying additional air flow rates Q_5

It can be observed from these figures that the relative distributions are almost independent from the additional air flow. Table 14 summarizes the properties of the distributions measured and the dilution factor:

$$\frac{C_N(Q_5)}{C_N(Q_5 = 10\ L/min)}$$

It can be seen in Table 14 that dilution factors up to 3.1 can be obtained without significant change of the airborne NP number size distribution.

Table 14: Effect of additional air flow (Q_5) on the CMMD and total concentration of airborne NP

Configuration	Q_5 (L/min)	CMMD (nm)	Ratio of number concentrations
1	10	248	-
	20	234	0.69
	30	233	0.50
	40	232	0.39
	50	231	0.32
2	10	93	-
	20	90	0.88
	30	86	0.69
	40	83	0.58
	50	81	0.51

3.7. Particle mixture (NP together with background aerosols)

One requirement of test facilities is the possibility to deliver well-known particle mixture containing combinations of the "primary" nanoaerosols together with particles representatives of background aerosols.

The initial CAIMAN configuration has been redesigned to produce not only the "primary" nanoaerosol (standard configuration) but also a known particle mixture containing combinations of the "primary" nanoaerosol and particles representatives of background aerosols. In the present work, preliminary tests have been carried out with NaCl particles as being representatives of background aerosols.

The Laskin-type nebulizer was chosen as generation system. The aerosol of NP produced within CAIMAN was mixed to an aerosol of NaCl crystals at the inlet of the ageing volume, as shown in Figure 38.

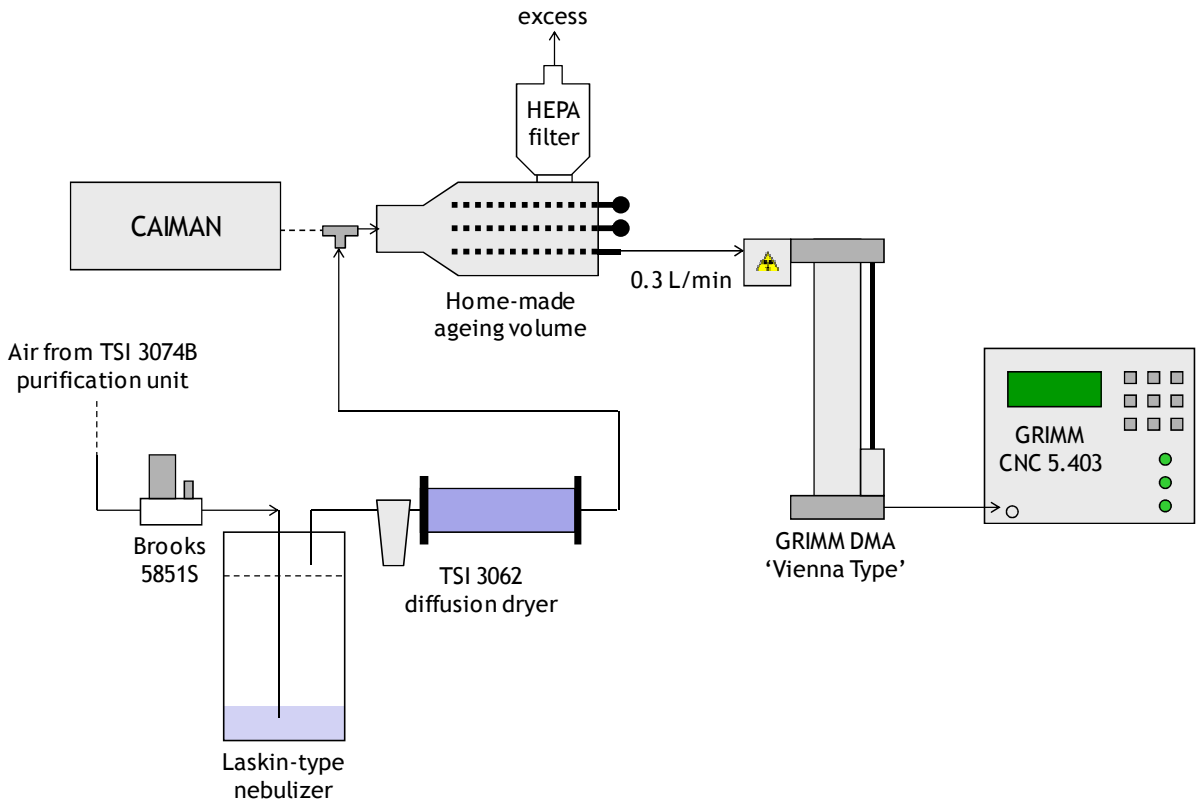

Figure 38: Set-up for the measurement of the number size distributions in the case of mixed aerosols

The Laskin-type nebulizer drawn in Figure 38 corresponds to a home-made generator based on the Laskin effect, described for example in the patent from Sabroske *et al.* [29]. It consists in a closed tank containing liquid, fed with a pressurized air source, which is connected to a Laskin type nozzle immerged in liquid. When pressurized air passes through the nozzle, a shearing process creates liquid droplets, which are then directed to the outlet of the tank and pass through a demister where the bigger droplets are removed.

To ensure complete drying of the droplets, the latter are directed through a diffusion dryer (filled with silicagel, TSI model 3062).

The preliminary experiments were performed with an aqueous solution of NaCl at a concentration of 0.5 g/L and an air flow rate of 20 L/min within the Laskin-type nebulizer. The influence of the height of liquid within the tank was investigated, as shown in Figure 39.

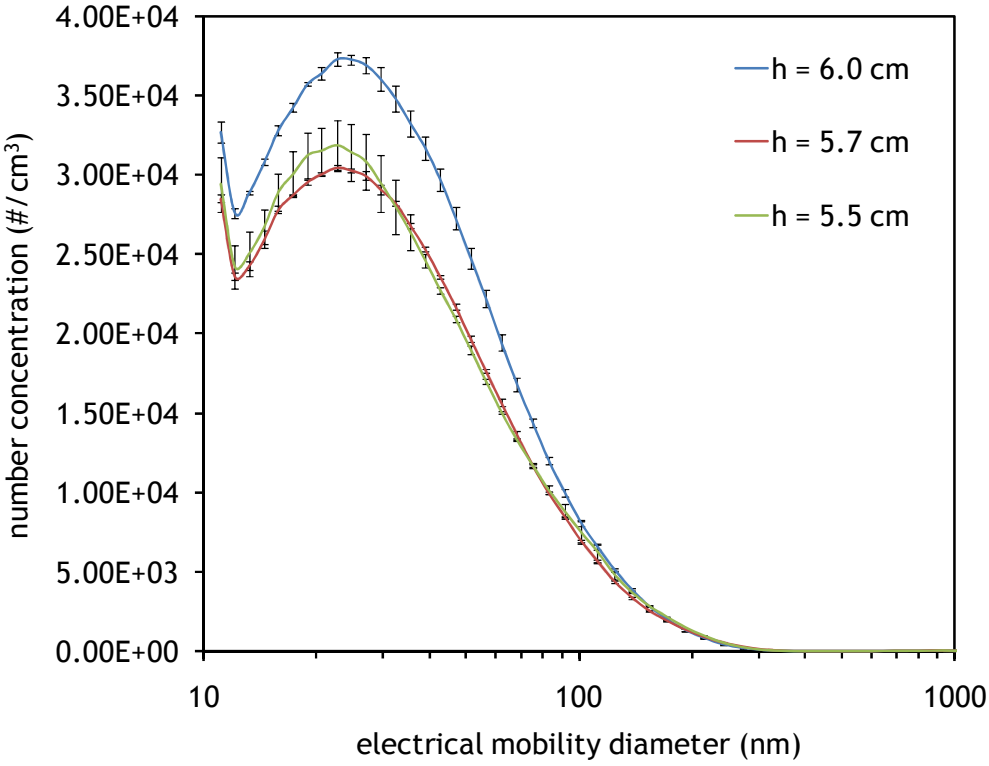

Figure 39: Effect of liquid height within the nebulizer on the number size distribution measured for NaCl

As an illustration, Figure 40 shows the number size distribution of a bimodal aerosol that has been obtained while using the Carbon electrodes (Q_1 = 2.5 L/min, Q_2 = 0 L/min, Q_4 = 1.5 L/min, Q_5 = 50 L/min, ω = 1000 a.u.) and generating NaCl particles (height of liquid 6.0 cm). In Figure 40, the finer mode (23 nm) corresponds to the NaCl particles and the larger one (350 nm) to the carbon particles.

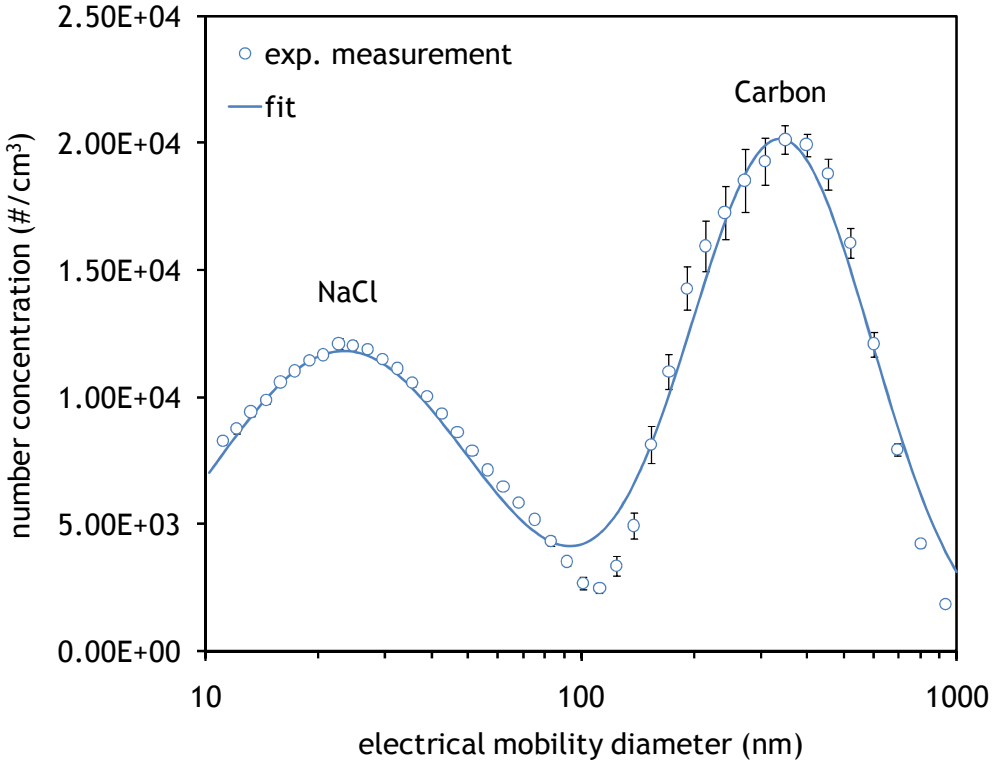

Figure 40: Number size distribution of the particle mixture obtained for Carbon electrodes and NaCl particles. The finer mode (23 nm) corresponds to the NaCl particles and the larger one (350 nm) to the carbon particles

4. Conclusion

In this report, the performances of the CAIMAN non-transportable facility have been evaluated.

The CAIMAN facility provides well-characterized “primary” nanoaerosols at known concentrations, sizes, shapes and mean charge levels. Within CAIMAN, nanoaerosols are produced by means of a spark-discharge generator (GFG-1000, PALAS). Until now, seven material electrodes have been used within CAIMAN: Carbon (delivered by PALAS), Aluminum (type 2071A), Copper, Silver, Constantane, Cu/Be and Cu/Co/Be.

The airborne NP characterized in this work present count median mobility diameters from 7 to 228 nm, with number concentrations varying from 1.7 10^6 to 1.8 10^7 #/cm^3.

The standard configuration of CAIMAN has been redesigned to produce not only the “primary” nanoaerosol but also a known particle mixture containing combinations of the “primary” nanoaerosol and particles representatives of background aerosol. In the present work, tests have been made with NaCl.

The output of the CAIMAN facility is now very consistent over long time intervals when operating under similar conditions. It indicates that repeatability is one of the important assets of the CAIMAN facility

Also, the CAIMAN facility has been confined in order to provide for the user safe working conditions against incidental releases of NP.

5. References

[1] Schwyn S, Garwin E and Schmidt-Ott A (1988). Aerosol generation by spark discharge. *Journal of Aerosol Science* **19**(5): 639-642.

[2] Helsper C., Molter W., Loffler F., Wadenpohl C., Kaufmann S. and Wenninger G. (1993). Investigations of a new aerosol generator for the production of carbon aggregate particles. *Atmospheric Environment* **27**: 1271-1275.

[3] Roth C., Karg E. and Heyder J. (1998). Do inhaled ultrafine particles cause acute health effects in rats? I: Particle production. *Journal of Aerosol Science* **29**(Suppl 1): S679-S680.

[4] Brown J.S., Kim C.S., Reist P.C., Zeman K.L. and Bennett W.D. (2000). Generation of Radiolabeled "Soot-like" Ultrafine Aerosols suitable for use in Human inhalation studies. *Aerosol Science and Technology* **32**: 325-337.

[5] Evans D.E., Harrison R.M. and Ayres J.G. (2003). The generation and characterisation of elemental aerosols for human challenge studies. *Journal of Aerosol Science* **34**: 1023-1041.

[6] Evans D.E., Harrison R.M. and Ayres J.G. (2003). The generation and characterization of metallic and mixed element aerosols for human challenge studies. *Aerosol Science and Technology* **37**: 975-987.

[7] Horwath H. and Gangl M. (2003). A low-voltage spark generator for production of carbon particles. *Journal of Aerosol Science* **34**: 1581-1588.

[8] Roth C., Ferron G.A., Karg E., Lentner B., Schumann G., Takenaka S. and Heyder J. (2004). Generation of ultrafine particles by spark discharging. *Aerosol Science and Technology* **38**: 228-235.

[9] Borra J.P. (2006). Nucleation and aerosol processing in atmospheric pressure electrical discharge: Powders production, coatings and filtration. *Journal of Physics D*, **39**: R19-R54.

[10] Byeon J.H., Park J.H. and Hwang J. (2008). Spark generation of monometallic and bimetallic aerosol nanoparticles. *Journal of Aerosol Science* **39**: 888-896.

[11] Tabrizi N.S., Ullmann M., Vons V.A., Lafont U. and Schmidt-Ott A. (2009). Generation of nanoparticles by spark discharge. *Journal of Nanoparticle Research* **11**(2): 315-332.

[12] Tabrizi N.S., Xu Q., van der Pers N.M., Lafont U. and Schmidt-Ott A. (2009). Synthesis of mixed metallic nanoparticles by spark discharge. *Journal of Nanoparticle Research* **11**(5): 1209-1218.

[13] Tabrizi N.S., Xu Q., van der Pers N.M. and Schmidt-Ott A. (2010). Generation of mixed metallic nanoparticles from immiscible metals by spark discharge. *Journal of Nanoparticle Research* **12**(1): 247-259.

[14] Bau S., Witschger O., Gensdarmes F. and Thomas D. (2009). Experimental study of the response functions of direct-reading instruments measuring surface-area concentration of airborne nanostructured particles. *Journal of Physics, Conference Series* **170**: 012006. DOI 10.1088/1742-6596/170/1/012006.

[15] Bau S., Witschger O., Gensdarmes F., Thomas D. and Borra J.-P. (2010). Electrical properties of airborne nanoparticles produced by a commercial spark-discharge generator. *Journal of Nanoparticle Research*, DOI 10.1007/s11051-010-9856-y.

[16] Marquard A., Meyer J. and Kasper G. (2006). Characterization of unipolar electrical aerosol chargers – Part I: a review of charger performance criteria. *Journal of Aerosol Science* **37**: 1052-1068.

[17] Marquard A., Meyer J. and Kasper G. (2006). Characterization of unipolar electrical aerosol chargers – Part II: Application of comparison criteria to various types of nanoaerosol charging devices. *Journal of Aerosol Science* **37**: 1069-1080.

[18] Schmidt-Ott A. (1988). New approaches to in situ characterization of ultrafine agglomerates. *Journal of Aerosol Science* **19**: 553-563.

[19] Schmidt-Ott A., Baltensperger U., Gäggeler H.W. and Jost D.T. (1990). Scaling behavior of physical parameters describing agglomerates. *Journal of Aerosol Science* **21**(6): 711-717.

[20] Shimada M., Seto T. and Okuyama K. (1994). Size change of very fine silver agglomerates by sintering in heated flow. *Journal of Chemical Engineering of Japan* **27**: 795-802.

[21] Weber A.P., Baltensperger U., Gäggeler H.W. and Schmidt-Ott A. (1996). In situ characterization and structure modification of agglomerated aerosol particles. *Journal of Aerosol Science* **27**: 915-929.

[22] Weber A.P. and Friedlander S.K. (1997). In situ determination of the activation energy for restructuring of nanometer aerosol agglomerates. *Journal of Aerosol Science* **28**: 179-192.

[23] Jang H.D. and Friedlander S.K. (1998). Restructuring of chain aggregates of titania nanoparticles in the gas phase. *Aerosol Science and Technology* **29**: 81-91.

[24] Nakaso K., Shimada M., Okuyama K. and Deppert K. (2002). Evaluation of the change in the morphology of gold nanoparticles during sintering. *Journal of Aerosol Science* **33**(7): 1061-1074.

[25] Ku B.K. and Maynard A.D. (2005). Comparing aerosol surface-area measurements of monodisperse ultrafine silver agglomerates by mobility analysis, transmission

electron microscopy and diffusion charging. *Journal of Aerosol Science* **36**(9): 1108-1124.

[26] Ku B.K. and Maynard A.D. (2006). Generation and investigation of airborne silver nanoparticles with specific size and morphology by homogeneous nucleation, coagulation and sintering. *Journal of Aerosol Science* **37**: 452-470.

[27] Cho K., Hogan C.J. and Biswas P. (2007). Study of the mobility, surface-area, and sintering behavior of agglomerates in the transition regime by tandem differential mobility analysis. *Journal of Nanoparticle Research* **9**: 1003-1012.

[28] Wang Y.Q., Liang W.S. and Geng C.Y. (2010). Shape evolution of gold nanoparticles. *Journal of Nanoparticle Research* **12**: 655-661.

[29] Sabroske K.R., Hoying D.A. and Rabe D.C. (1996). Laskin nozzle particle generator. US patent number 5 498 374.